Title
Block copolymer electrolytes for lithium batteries

Author
Hudson, William Rodgers

Publication Date
2011

Peer reviewed|Thesis/dissertation

Block Copolymer Electrolytes for Lithium Batteries

By

William Rodgers Hudson

A dissertation submitted in partial satisfaction of the

requirements for the degree of

Doctor of Philosophy

in

Chemistry

in the

Graduate Division

of the

University of California, Berkeley

Committee in charge:

Professor Jeffrey Long, Chair
Professor Marcin Majda
Professor John Newman

Spring 2011

Abstract

Block Copolymer Electrolytes for Lithium Batteries

by

William Rodgers Hudson

Doctor of Philosophy in Chemistry

University of California, Berkeley

Professor Jeffrey Long, Chair

Increasing interest in renewable energy technologies has recently brought compact and cost-effective energy storage into the spotlight. A wide variety of applications could benefit from an appropriate high-energy storage medium capable of efficiently collecting and releasing electrical energy. In this work, the lithium metal battery is introduced as one of the most exciting candidates with the potential to fill this need. In chapter one, today's leading battery solution is explored and compared to the lithium metal cell, and challenges to cycle and calendar life in each system are explained. In particular, the advantages and limitations of the state-of-the-art Li-ion chemistry, including its graphite-based negative electrode, are discussed. Specific challenges to the implementation of metallic lithium – the negative electrode with the highest possible specific energy – are also presented, with the pervasive growth of catastrophic lithium dendrites being the most significant obstacle to its success. An active body of investigation into the formation of these dendritic microstructures in lithium metal cells and various strategies toward eliminating them are introduced. Finally, with support from recent research, we propose that the hard-soft, nanostructured block copolymer electrolyte, poly(styrene-block-ethylene oxide), (PS-b-PEO), represents a fundamentally new approach toward stopping lithium dendrite failure and, in so doing, realizing a metallic lithium anode as part of a stable higher-energy rechargeable battery.

The second chapter presents a complete set of fundamental transport measurements on the solid electrolyte, PS-b-PEO containing the lithium bis(trifluoromethane)sulfonimide (LiTFSI) salt. The LiTFSI mutual diffusion coefficient, measured by restricted diffusion in symmetric lithium cells, is reported along with the ionic conductivity, measured by potentioelectrochemical impedance spectroscopy, for a wide range of salt concentrations at 80 °C. A comparison between these results and those for the homopolymer-PEO system are also discussed. In addition, a straightforward approach toward measuring the lithium transference number in solid electrolyte samples is reported and compared to various existing methods. The transference measurement reported herein depends on an

experimental determination of the limiting current, which is undertaken for a range of salt concentrations, also in lithium symmetric cells at 80 °C.

In the third chapter, the focus turns to practical batteries containing lithium metal as a negative electrode and lithium iron phosphate ($LiFePO_4$) as a positive electrode. An extensive electrochemical characterization on batteries with these electrodes and the solid electrolyte PS-b-PEO containing LiTFSI is first reported. In cells with high specific energy, exceptional electrochemical and high-temperature stability is demonstrated over months of repeated charge and discharge cycling. Data collected at charge/discharge rates in the appropriate range for electric vehicle applications (i.e., C/2, which is defined as the current necessary to fully charge or discharge a cell in 2 hours) are compared to data collected on comparable homopolymer-based cells. In order to project ultimate cycle and calendar life limitations, coulombic and energy efficiency measurements are taken for each system, and electron micrographs demonstrate the unprecedented reversibility of the metallic lithium electrochemical reaction in all-solid-state batteries containing the block copolymer electrolyte.

Finally, chapter four describes high-resolution *in situ* concentration mapping of dissolved LiTFSI in working lithium symmetric cells containing the same block copolymer electrolyte. By synchrotron scanning transmission X-ray microscopy (STXM), performed on all-solid-state batteries, real-time ion composition data, generated by quantitative X-ray absorption measurements, are reported under galvanostatic charge and discharge conditions. In particular, nanometer-resolution fluorine 1s absorbance data within working batteries are converted to Li^+ concentration maps to elucidate the evolution of ion composition changes in cells during cycling. Furthermore, a general approach toward accurate, *in situ*, fundamental transport measurements, including a representative measurement of the lithium transference number for LiTFSI in PS-b-PEO, is reported. We believe this technique represents a seminal effort toward a general method of *in situ*, nanoscale, soft-X-ray characterization of lithium-based batteries that can be extended to the investigation of other electrolytes as well as to a wide variety of electrode materials for electrochemical systems of all types.

Table of Contents

Acknowledgements

First and foremost I would like to thank my advisor, Jeff Long, for his consistent guidance and support. I am forever indebted to him for taking me on as a student and nurturing me through this process.

I owe more than a little gratitude to my parents, Kate and Dave, for their bottomless love, frequent encouragement, and tender support during not just this phase but all the steps in my life, whether or not I thought I needed them! My brothers, Ty and Peter, have always inspired and challenged me. I thank them, too, for putting up with me over the years.

Many others are owed similar appreciation for their help in innumerable ways, and although I cannot mention all by name, a few have made particularly important contributions that I wish to recognize. My colleagues, mentors, and friends, Mohit Singh and Hany Eitouni have nurtured me both intellectually and personally through this journey, which has seen its share of ups and downs. I will forever appreciate their patience and understanding and, perhaps most of all, their leap of faith that embarking on this journey was a worthwhile undertaking. I would like to thank Nitash Balsara both for his advice and direction as well as for his trust in me from the start. My other colleagues and friends at UC Berkeley, Seeo, and myriad other places have also been helpful and understanding along the way. To all of them, for everything they have done, I say thanks.

Lastly, I wish to thank my girlfriend, Melissa, for challenging me, motivating me, maintaining my sanity, and, most importantly, keeping me around during the last several years. How and why you did it, I won't know, but thank you!

Chapter 1

Introduction

1.1. Background

Considerable recent effort has been put toward the advancement of renewable energy strategies to reduce our reliance on petroleum as the world's primary fuel. That effort, which will almost certainly utilize multiple sources of power, must include the development of versatile and inexpensive energy storage to be successful. For example, promising energy generation technologies dependent on the solar flux – including solar and wind power – as well as other renewable methods that produce power on a timescale out of sync with variable energy usage, will benefit from, if not altogether require, a large-scale storage solution. Mobile power delivery, including vehicular transportation, also depends on a new storage solution if it is to be freed from its long dependence on fossil fuels. Furthermore, improving energy utilization efficiency, which will be critical to reaching global sustainability, requires more convenient energy transfer among what are sure to be multiple production and utilization approaches. With that in mind, a practical storage solution that can enable widespread growth of non-petroleum-based fuels must satisfy a number of challenging criteria: it should be compatible with the electrical grid, have high utilization efficiency, be robust to significant time and repeated use, require low capital and amortized cost, and present little unmanageable health risk or physical danger. There is no question that these are a set of impressive challenges. However, it is clear that the realization of a technology that meets them will profoundly impact the way that humans generate and use energy well into the future.

Ever since 1800 when Alessandro Volta discovered that chemical energy could be converted into electric current, batteries have been investigated as an energy storage medium that could meet these criteria. As Volta demonstrated with his voltaic pile, the electrochemical cell – or battery – controllably converts the energy contained in chemical bonds to an electric current according to the electromotive force (emf). This emf, expressed in Volts (V), or Joules per unit of electrical charge (Coulomb, C), is analogous to the pressure of water in a pipe and depends on the potential difference among chemical bonds within electrode materials of different composition. With his primitive cell, Volta generated an electric current between plates of zinc and copper, but a useful battery can be constructed of almost any two dissimilar electrode materials if separated by a suitable, ionically conducting electrolyte. Easily compatible with our existing electrical grid, batteries can be used to store and release energy repeatedly and with high efficiency.

Although batteries have existed for over two centuries, they still do not find widespread use in many important storage applications. For example, they have made recent inroads into automobiles but remain dangerous, heavy, and expensive, making widespread electrification of the vehicle fleet a significant challenge.[1] Other large-scale battery

opportunities that have generated recent academic and commercial interest, including backup for telecommunications, grid-tied utility storage, and distributed-energy storage, all demand low amortized cost and thus high energy per raw material cost, in addition to exceptional calendar- and cycle-life to be successful. These applications, in addition to electric vehicles, need cheaper, longer-lived, higher-energy rechargeable batteries.

For perspective, in Table 1.1 the energy content of a few existing secondary (rechargeable) battery technologies is listed along with their cost and lifetime. It can be seen that the Li-ion cell is the best existing system where high energy density is required, its commercial introduction in 1991 being a major breakthrough for the battery industry.[2] The Department of Energy goals for electric vehicle batteries are also included in Table 1.1, with the most difficult challenges being system-level specific energy, cost, and operating lifetime. In Figure 1.1, these and a few other battery chemistries are related according to their energy density versus specific energy, with the smallest and lightest chemistries located in the top right corner. For comparison, it should be noted that gasoline has an energy density of 9668 Wh/L and 12335 Wh/kg, approximately 20 times the energy density and 50 times the specific energy of today's leading rechargeable battery system. While the efficiency of a gasoline-powered combustion engine is lower than that of a contemporary electric motor, it should still be recognized that a monumental challenge exists in attempting to replace gasoline as our primary fuel, especially in weight and volume-sensitive applications. Nevertheless, batteries are leading candidates to play an important role in the transition to a renewable energy future; and not surprisingly, they are experiencing a recent renaissance of interest and research.

Table 1.1. Energy, cost, and cycle life of several rechargeable battery technologies

	Specific Energy	Cost per Wh	Cycle Life	Lifetime	Ref
Lead Acid	35 Wh/kg	0.1 $	500+ cycles	2-3 yrs	[1,3]
Ni-MH	100 Wh/kg	0.4 $	1000+ cycles	>10 yrs	[1,4-6]
Li-Ion	220 Wh/kg	0.5 $	1000+ cycles	>3 yrs	[1,2,7]
Electric vehicle target	150 Wh/kg*	0.15 $	1000 cycles	10 yrs	[1]

*system level, including cooling, battery management, and all electrical and mechanical components

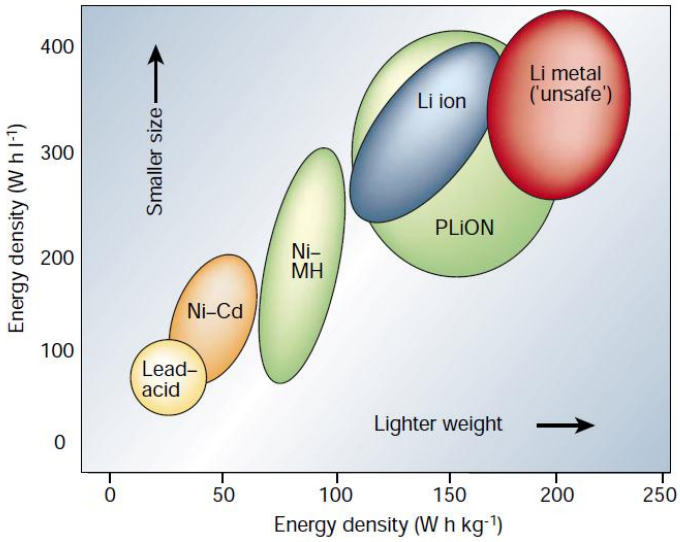

Figure 1.1. Energy density comparison among various battery chemistries.[8]
Several rechargeable battery technologies are compared in terms of their available energy per mass and volume. Li metal, which is described as inherently unsafe, has the highest possible specific energy and volumetric energy density. Improving the safety of this system would require the replacement of conventional organic, liquid electrolytes. Figure reproduced from reference 8.

At its most basic, the electrochemical cell is made up of three components: two conducting electrodes and an electrically-insulating but ionically-conducting electrolyte (Figure 1.2). Potential energy is stored in the bonds of the negative electrode and converted to useable, electrical energy upon completion of an external electrical circuit, which permits the flow of electrons for the purpose of doing work. These electrons are driven by an electric field spontaneously to the positive electrode, as water driven through a pipe down a pressure gradient, where they may participate in the formation of new, more stable bonds. The negative and positive electrodes, zinc and copper in the first battery, but otherwise generic, are composed of chemical constituents that can be oxidized or reduced, respectively, to generate or consume electrons. When the external circuit is completed, the electrochemical reactions proceed spontaneously: the negative electrode functions as an anode, meaning that oxidation takes place to produce electrons and cations, while reduction occurs at the cathode, with electrons and cations combining in a concomitant half-reaction. In this configuration, the electrochemical system is referred to as a galvanic cell. On the other hand, if energy is put into the system to increase artificially the net cell potential, the electrochemical reaction can be run in reverse, in which case it is called an electrolytic cell. Therein, the negative electrode performs reduction and is called the cathode, while the positive electrode performs oxidation and is called the anode. Rechargeable batteries are

those that can operate in both directions, having the ability to charge (electrolytic cell) and discharge (galvanic cell) reversibly over multiple cycles.

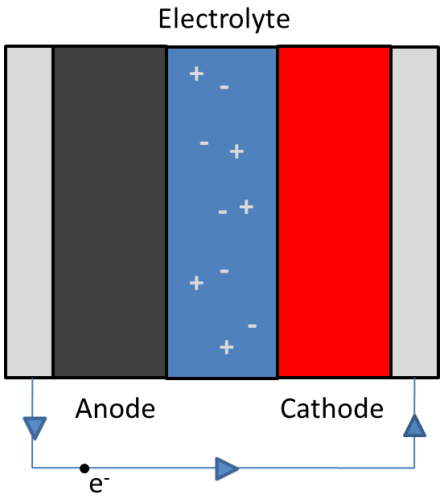

Figure 1.2. Graphical representation of a generic electrochemical cell. A generic electrochemical cell is composed of three parts: a negative electrode (anode during discharge), a positive electrode (cathode during discharge), and an electrically-insulating electrolyte. The electrolyte contains a dissolved salt in order to transport ionic charge within the cell, while electrical current is carried through an external circuit where it is available to do useful work.

Thermodynamically, the maximum work that can be done by an electrochemical system depends on the free-energy difference between the bonding electrons in each electrode, and is described by

$$\Delta G = -nFE \tag{1.1}$$

where G is the Gibbs free energy, F is Faraday's constant, n is the moles of electrons, and E is the cell potential in Volts. Herein, a negative or spontaneous electrochemical reaction, the net sum of half reactions occurring at each electrode, has a positive electrochemical potential. Unlike conventional redox reactions, however, the half reactions in an electrochemical system must remain physically separate. That is to say, in order for the electrons to power electrical devices, they must not pass directly between reductant and oxidant.

It is this physical separation that necessitates the third component of every electrochemical cell: the ion-conducting electrolyte. By virtue of its high electrical resistivity, the electrolyte inhibits the internal flow of electrons, meanwhile facilitating transport through the cell of charge via dissolved ions. The ion flux, therefore – sustained by oxidation at the anode surface – provides the chemical reactants for a reduction half-reaction at the cathode, completing the overall redox chemistry. High ionic conductivity is required to permit ion transport, as ionic current through the electrolyte must equal in magnitude the electronic

current outside the cell. Sandwiched between high- and low-potential negative and positive materials, therefore, the electrolyte is the ion pipeline for the transfer of energy between source and sink.

While these three components – two electrodes and an electrolyte – are necessary and sufficient to define an electrochemical cell, great variation can exist between cells, both in the chemistry of the electrode materials as well as the electrolyte interfacing between them. The ideal electrochemical cell contains chemical species with the largest possible difference in electrochemical potential. In general, species with high-energy, unstable bonds, paired with more stable, low-energy materials will produce a system with the highest voltage. Because the energy of a battery is given by the product of voltage and capacity, higher voltage, i.e., energetic driving force per electron, tends to increase the energy storage capability. In addition to cell voltage, however, other factors have considerable value to practical batteries. The second term in the energy equation, battery capacity, is defined as the total electrical charge that it can store. While capacity can be increased by adding electrode material, capacity density is inherent to material choice. In situations where space and weight are at a premium, the total volumetric and gravimetric energy densities are often the most important features of an electrochemical system. These are given by

$$E = \frac{CV}{g} \tag{1.2}$$

and

$$E = \frac{CV}{L} \tag{1.3}$$

where V is the average system voltage, C is the total capacity in coulombs, g is the system mass, and L is its volume. Typically, materials with low atomic mass on opposite sides of the periodic table make the most appealing candidates for battery electrodes.

In fact, of all materials, lithium metal, which is not only the third lightest element, but also has the lowest half-cell reduction potential of any element, is perhaps the most ideal of all. It is for this reason that lithium has generated great interest in recent decades as a negative electrode.[2,8-12] When used in its elemental form, lithium participates in the following oxidation reaction:

$$\mathrm{Li} \rightarrow \mathrm{Li}^{+} + \mathrm{e}^{-} \tag{1.4}$$

with a standard reduction potential of -3.05 V (vs. a normal hydrogen electrode, NHE). When paired with a suitable positive electrode material that can be reduced along with the lithium cation and free electron – products of the reaction above – a lithium-based battery can be made.

Early attempts at rechargeable lithium systems utilized high-potential metal oxides such as CoO_2 as the positive electrode material.[2] Cobaltate readily and reversibly intercalates lithium according to

$$CoO_2 + xLi^+ + xe^- \rightarrow Li_xCoO_2 \quad (1.5)$$

with a standard reduction potential that varies with x above, around 0.8 V (vs. NHE). Similar oxides including those of Mn and Ni have also found common use in commercial lithium-based batteries.[7,13,14] The crystal structure of these intercalation compounds is layered (α-$NaFeO_2$), such that alternating planes of oxygen atoms are separated by metallic species, M, from the generic formula $LiMO_2$.[15] In the planes between successive O layers, Li^+ ions reversibly intercalate with high diffusivity. Other intercalation structures, including the spinel, $LiMn_2O_4$,[16] and the olivines described by $LiMPO_4$,[17-19] where M can be Fe, Mn, Co, or Ni, are also known to be effective. Much recent interest has focused on the latter due to the strength of their P-O bond and, therefore, their structural and thermal stability.[20] Furthermore, $LiFePO_4$, which is synthesized from abundant, nontoxic starting materials, has continued to gain momentum in the electrochemical community since the initial report of its synthesis by Padhi *et al.* in 1997.[19] Similar to cobaltate, lithium iron phosphate undergoes a reversible intercalation half-reaction given by

$$FePO_4 + xLi^+ + xe^- \rightarrow Li_xFePO_4 \quad (1.6)$$

with a flat reduction potential (between $0.02 < x < 0.9$) of 0.37 V.[21] The nominal cell potential of a battery composed of Li metal and an intercalation compound such as $LiFePO_4$ is determined by the difference of its negative and positive half-cell potentials, which for the Li/$LiFePO_4$ electrochemical couple is 0.37 V – -3.05 V, or 3.42 V.

It was found that for a lithium-based electrochemical system such as Li/$LiFePO_4$, organic electrolytes based on alkyl carbonates, such as propylene carbonate (PC) or diethylcarbonate (DEC),[2] make effective ionically conducting electrolytes. Various mixtures of these low-boiling solvents (e.g., PC/DEC) have found success, but any suitable electrolyte could be used that meets the following criteria: 1. It must have the sufficient dielectric properties to dissolve a lithium salt and allow facile transport of positive charge via the Li^+ cation. 2. It must be chemically and electrochemically stable toward oxidation and reduction, coming into physical contact with both positive and negative electrodes. 3. It must be thermally stable in the operating environment. To date, the alkyl carbonates have been the most successful electrolytes in terms of these criteria. They are nonreactive with many common lithium-intercalating positive electrodes, having reported oxidation potentials exceeding 4.5 V versus Li/Li^+.[22,23] Although they are not reductively stable at the lithium metal surface,[24] they can also form a self-limiting passivation film,[23,25] which makes them kinetically stable at least under some conditions against a lithium anode. And, due to their relatively low viscosity and high dielectric properties, appropriate mixtures have sufficient ionic conductivity to facilitate adequate charge transport at temperatures as low as -40 °C. While conductivity, and thus, battery performance typically increase with

temperature, above 45 °C adverse electrode-electrolyte reactions can significantly reduce cell lifetime,[26-29] which means these liquid electrolytes have a useful operating window of approximately 85 degrees.

Of course, in addition to a suitable solvent, charge transport also requires an appropriate ionized lithium salt that is compatible with the electrodes of interest. Lithium salts with large, charge-delocalized anions have been the most successful due to their high degree of dissociation and thus charge-carrier density, which factors into the ionic conductivity according to

$$\kappa = F^2 z^2 \mu c \tag{1.7}$$

where F is Faraday's constant, z is the ionic charge, μ is the mobility, and c is the ion concentration. Lithium hexafluorophosphate ($LiPF_6$) is used in the majority of commercial Li-ion systems, although other anions, including perchlorate, hexafluoroarsenate, and tetrafluoroborate, have been used with varying success.

The first lithium-based rechargeable systems, therefore, were constructed from a metallic-lithium negative electrode, a porous-plastic, insulating separator swollen with an organic liquid electrolyte containing a dissolved lithium salt, and a porous, composite electrode made up of a lithium intercalation material[30] (Figure 1.3). This system, in fact, is very close to that found in the majority of rechargeable batteries used today in consumer electronic devices, including laptops and cell phones, as well as many recently-released electric and hybrid-electric vehicles. However, very early on it was found that the metallic-lithium electrode could not be safely and reliably cycled over time. Despite the quasi-stability of lithium metal-liquid electrolyte passivation film, it has been demonstrated that the lithium electrode has a strong tendency to form high-surface area microstructures upon repeated plating and stripping;[31-35] these structures, under common conditions of use, readily grow into filaments that can reach across the cell to cause dangerous and often-catastrophic cell failure. In fact, the electrical shorts that occur produce significant local heating, which can initiate aggressive exothermic "runaway" reactions between anode, cathode, and electrolyte, and in many cases cause fires and explosions.[36] Furthermore, even before dramatic cell-death events such as these occur, "mossy" lithium structures are known to form under even benign charge/discharge conditions.[35] Such structures, driven by local electric field inhomogeneity, are accelerated by lithium surface roughness and other local variations in the system,[37] and are most likely during fast-charge conditions,[38] which are necessary in many practical applications. When formed, mossy lithium presents a large surface area for electrolyte reduction and the build-up of a resistive solid-electrolyte interphase (SEI), which reduces cell performance and leads to rapid, if not dangerous, cell failure.[31]

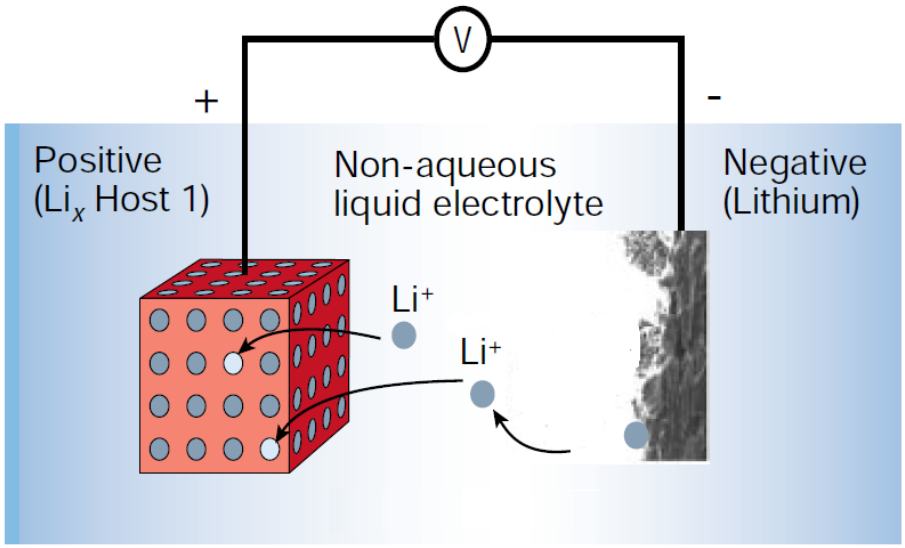

Figure 1.3. Lithium-metal/intercalation-electrode battery structure.[8] A graphical representation of a lithium metal/positive-intercalation electrochemical system shows lithium ions, produced by oxidation at the metallic electrode surface, passing through an organic electrolyte to host sites in a crystalline positive electrode. Figure reproduced with modifications from Reference 8.

It is these frequent failure modes that prompted investigation into today's widely successful Li-ion cell, introduced commercially in 1991 by Sony Corporation.[2] In order to avoid the dangerous cell failures caused, in part, by lithium metal, the Li-ion cell replaces the metallic lithium electrode by a porous-composite material similar in structure to its positive counterpart (e.g., $LiCoO_2$), but made up of low-potential graphite rather than a high-potential oxide. This configuration (Figure 1.4), sometimes known as the "rocking-chair" system because of the two intercalation electrodes between which lithium ions are shuttled, has become the standard high-energy rechargeable system. The electrochemical half-reaction taking place at the graphite negative electrode has an average potential of approximately -2.90 V (vs. NHE) and can be described by

$$C_6 + xLi^+ + xe^- \rightarrow Li_xC_6 \qquad (1.8)$$

Graphite, unlike lithium metal, allows for the facile and reversible intercalation of lithium ions from an organic liquid electrolyte such as PC:DEC (with 1 M $LiPF_6$), which, similar to the layered oxides, is known to be stable over hundreds of cycles. That being said, because of its low potential vs. Li/Li^+ (appx. 0.15 V), conventional liquid electrolytes are not thermodynamically stable at the graphite electrode surface. In fact, very few chemical structures are nonreactive in this aggressive reducing environment.[23] Like the resistive SEI formed against the metallic-lithium surface, therefore, a passivation film also forms on the graphite surface; but, in this case, it can be controlled by careful charging in the first cycle and occurs in a complex but relatively predictable fashion.[39] That is to say, unlike the

lithium metal electrode, where fresh lithium must be deposited every charge cycle, once a passivation film has formed on the graphite electrode, it remains quasi-stable under typical conditions of use. Abusive conditions including low-temperature or fast-charging as well as high-temperature operation can cause more rapid failure,[40,41] but this electrode has otherwise been quite resilient to competition from other negative electrode materials.

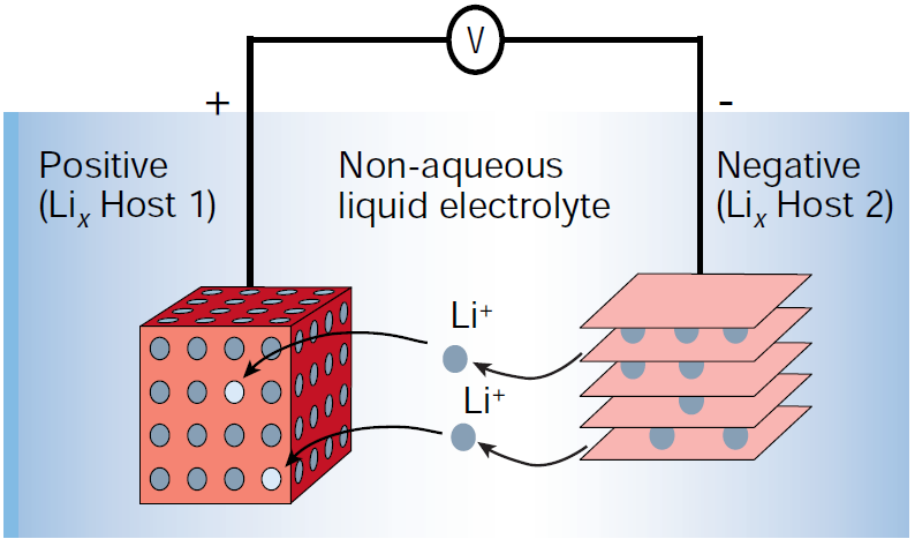

Figure 1.4. Dual-intercalation battery structure. A graphical representation of a negative-intercalation/positive-intercalation electrochemical system depicts a negative electrode composed of alternating planes of material into and out of which lithium ions may reversibly diffuse. Figure reproduced from Reference 8.

Despite its considerable success, however, the graphite-based anode sacrifices significant specific energy and energy density relative to a comparable lithium-metal cell. Research, therefore, continues aggressively to supplant this material with a higher-energy alternative. A comparison between lithium metal and several negative electrode candidates either in use or under investigation can be seen in Table 1.2, along with the theoretical and practical specific energy and volumetric energy density of those same materials (Figures 1.5 and 1.6). Energy quantities are calculated from specific capacity or volumetric capacity multiplied by the nominal cell voltage assuming a positive electrode with a nominal potential of 3.8 V versus Li/Li^+, as per equations 1.2 and 1.3. This positive electrode potential represents a generic cathode material such as $LiCoO_2$. As can be seen, even when excess lithium (3x the required amount) is incorporated to mitigate gradual loss of lithium capacity and to provide sufficient material for processing and current collection, the lithium metal electrode retains a practical gravimetric energy advantage more than 4 times that of a graphite electrode, as well as a practical volumetric energy advantage of almost 2-fold. It should be noted that in contrast to many reports of specific capacity for the electrode materials included, in Table 1.2 specific capacity is calculated from the active

mass at full state-of-charge (SOC), i.e., highest lithium content, for better comparison with lithium metal (which would have an infinite specific capacity if referenced at zero SOC because all the electrochemically active lithium would be stored in the positive electrode). Also, the practical active loadings and practical active densities listed below reflect the need for additional material – conductive additive and polymeric binder – in nonmetallic, intercalation electrodes as well as the pore space (ca. 30%) they require for use with liquid electrolytes. Furthermore, for appropriate comparison, the addition of a heavy, expensive current collector (most often copper) must also be considered in the final accounting, although it is not included here. Lithium metal, to its advantage, requires no additional material, porosity, or current collection and will therefore fare even better in mass and volume comparisons with alternative electrode materials.

Table 1.2. Characteristics of four negative electrode materials

Material	**Lithium**	**Graphite**	**Lithium Titanate**	**Silicon**
Chemical Formula	Li	LiC_6	$Li_7Ti_5O_{12}$	$Li_{22}Si_5$
Nominal Half-cell Potential (V vs Li/Li^+)	0	0.15	1.55	0.5
Lithium Equiv per Formula Unit	1	1	3	22
Practical Lithium Equiv	1	1	3	11
Formula Mass (g/mol)	6.941	79.006	479.917	293.134
Density (g/mL)	0.535	2.20	3.73	2.31
Specific Capacity (mAh/g)	3862	339	168	2012
Volumetric Capacity (mAh/mL)	2066	746	627	4647
Practical Active Loading [wt%]	33 (3x)	90	80	80
Practical Active Density [vol%]	33 (3x)	60	40	50

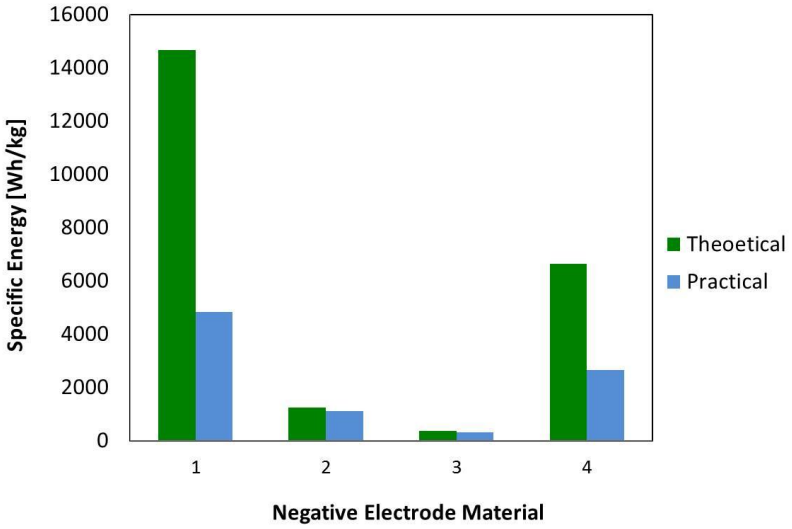

Figure 1.5. Specific energy of four negative-electrode materials. Theoretical and practical specific energy is compared for four common negative electrode materials considered for lithium-based batteries. 1 is Li metal, 2 is LiC_6, 3 is $Li_7Ti_5O_{12}$, and 4 is $Li_{22}Si_5$. Specific energy is calculated from equation 1.2, using the nominal potential and the theoretical or practical specific capacity from Table 1.2. For comparison, a representative but generic cathode material with a nominal potential of 3.8 V (vs. Li/Li^+) is assumed.

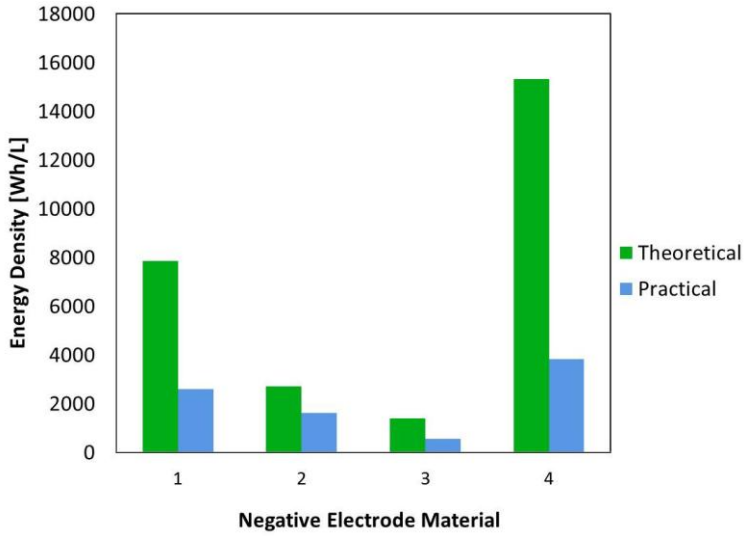

Figure 1.6. Volumetric energy density of four negative-electrode materials. Theoretical and practical volumetric energy density is compared for four common negative electrode materials considered for lithium-based batteries. 1 is Li metal, 2 is LiC_6, 3 is $Li_7Ti_5O_{12}$, and 4 is $Li_{22}Si_5$. Energy density is calculated from equation 1.3, using the nominal potential and the theoretical or practical volumetric capacity from Table 1.2. For comparison, a representative but generic cathode material with a nominal potential of 3.8 V (vs. Li/Li^+) is assumed.

Many efforts to avoid the use of the low-energy graphitic electrode have focused on replacing or supplementing the conventional liquid electrolyte with a material that might fare better in combination with lithium metal. Polymer electrolytes, with higher modulus than liquid electrolytes confer several potential advantages to a practical lithium-based battery.[42] In addition to their added mechanical strength, they tend to have better thermal stability, lower side-reaction kinetics, as well as improved processability.[10,11,43-46] Candidate solid conductors have centered on rubbery, alkoxy polymers that readily coordinate lithium ions and have low glass-transition temperatures, which, via fast chain dynamics, helps facilitate rapid ion conduction. The most studied and best understood of these polymers is poly(ethylene oxide) (PEO). Some of the earliest work on PEO electrolytes was performed in the 1970s and 1980s by Armand and coworkers, who discovered that lithium salts could be readily dissolved and transported by PEO.[47] This crystalline polymer melts above ca. 65 °C and has reported ionic conductivities in the range of 1×10^{-4} to 1×10^{-3} S/cm at a practical operating temperature of 80 °C,[48] depending on the lithium salt. Typical salts have incorporated mostly large, stable anions such as bis(oxolato)borate (LiBOB), triflate, and bis(trifluoromethane)sulfonimide (TFSI) in order to impede anion motion during polarization. While PEO has been a reasonably successful electrolyte, generating much academic and even commercial interest over the past several decades, lithium dendrite growth continues to plague this and related systems.

Other approaches toward electrolyte compatibility with lithium metal have focused on the introduction of passivating additives to conventional liquid electrolytes in order to control the production of electrolyte decomposition products and thus the formation of a stable SEI layer. Self-polymerizing compounds such as vinylene carbonate have been studied along with other passivating molecules including fluoroethylene carbonate and phosphoric acid.[49,50] In addition, ionic liquids, which have the advantage of low vapor pressure and low flammability, have been used either alone or in combination with other liquid or polymer electrolytes to improve lithium-plating behavior and to improve thermal stability.[32,51,52] For example, recent work by Bhattacharyya *et al.* has shown that 1-butyl-methylpyrrolidinium bis(trifluoromethane)sulfonimide with LiTFSI reduces the onset of dendrite formation as compared to other ionic liquids such as 1-ethyl-3-methylimidazolium tetrafluoroborate with $LiBF_4$.[32] Despite these attempts, however, no rechargeable lithium metal batteries are found on the market today.

Between 2003 and 2005, Monroe and Newman published several theoretical treatments of lithium dendrite formation and argued that it is the sheer modulus of an electrolyte material that dictates the formation energetics of lithium dendrites.[37,38,53] Their theory suggests that a sufficiently hard electrolyte could make it energetically unfavorable for a dendrite to protrude into the space otherwise occupied by electrolyte material. Conventional materials including liquid electrolytes, ionic liquids, as well as commonly-used conducting polymers including PEO, are orders of magnitude too soft to resist effectively the persistent growth of lithium microstructures. It was theorized that a suitably hard material requires a sheer modulus approximately twice that of lithium metal in order

to prevent interfacial roughening altogether.[53] That number exceeds 1 GPa. For comparison, conventional ion-conducting polymers like PEO have sheer moduli less than 1 kPa, or closer to 1 Pa at useful operating temperatures, which is larger than liquid electrolytes but still many orders of magnitude too low to stop dendrite-induced cell failures.

The challenge that prevents the discovery of alternative conducting polymers with higher modulus than PEO – approaching 1 GPa – but comparable or better ion conduction, emerges from the coupling of these properties in conventional homopolymer systems. In fact, ion conduction in rubbery polymers like PEO is known to be mediated by the movement of the polymer chains themselves,[45,48,54] such that any attempt to increase rigidity by modification of molecular architecture will reduce chain reptation and thus impede ion motion. A tradeoff exists which prevents polymer electrolyte stiffening without a significant reduction in conducting efficacy. As depicted in Figure 1.7, the mechanism of Li^+ conduction is predominantly shuttling by the polymer chain(s) to which it is coordinated, as opposed to longer-distance ion hopping between coordination sites.

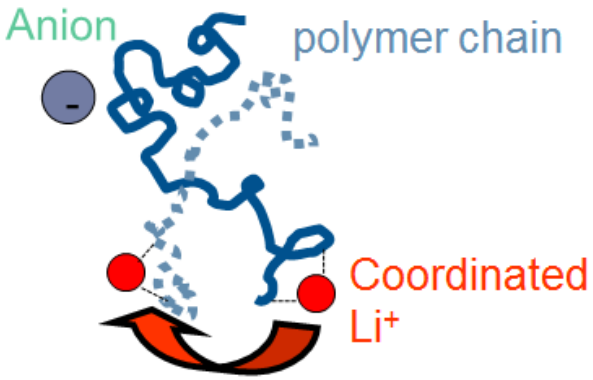

Figure 1.7. Polymer-mediated lithium ion transport in polymer electrolytes. Lithium conduction in solid polymers is mediated by the motion of individual polymer chains. The small lithium cation is tightly coordinated to the polymer backbone and depends on chain reptation for large-scale transport.

In 2007, Singh and coworkers for the first time overcame this limitation by synthesizing a block copolymer-based electrolyte, composed of two vastly different polymeric components, in order to replace the homopolymer electrolyte altogether.[55] They retained a PEO component as the conducting segment, and to it covalently attached a hard, non-conducting polystyrene (PS) chain to provide bulk structural rigidity. This nanostructured material, when composed of roughly equal volumes of hard and soft phase, self-assembles into channels of alternating lamellae with a length-scale on the order of tens of nanometers, much smaller than that of a protruding dendrite. The representative nanostructure formed by PS-b-PEO, visualized by transmission electron microscopy (TEM), can be seen in Figure

1.8, where contrast is enhanced by RuO_4 staining.[55] The alternating channels of soft, conducting phases in this material allow passage of lithium ions, while the hard, glassy mechanical regions act like molecular scaffolds, impeding solid lithium microstructures from growing through the electrolyte layer.

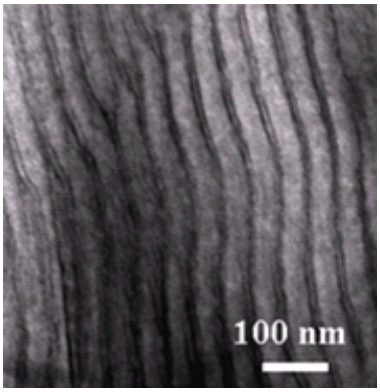

Figure 1.8. Transmission electron micrograph of a microphase-separated block-copolymer electrolyte.[55] A transmission electron micrograph of lamellar poly(styrene-block-ethylene oxide) (PS-b-PEO) shows self-assembled microphase separation typical of block copolymers with equal volume fractions of dissimilar chemical components. In this image, reprinted from Reference 55, contrast is enhanced with RuO_4 staining.

While the conductivity of PS-b-PEO was sacrificed relative to homopolymer PEO, a much-more impressive increase in mechanical strength was gained. In fact, the conductivity decrease was about a factor of 3 as compared to homopolymer PEO, while the storage modulus enhancement exceeded 3 orders of magnitude,[55] governed almost entirely by the PS component. To demonstrate the mechanical advantage of the nanostructured electrolyte, Figure 1.9 illustrates the in-phase and out-of-phase sheer moduli of PEO (MW = 20 kDa) and PS-b-PEO (MW = 61 kDa, 59:41 PS:PEO wt%) at 90 °C.[55] The in-phase modulus represents the storage or elastic component, while the out-of-phase modulus represents the loss or viscous component. A dramatic increase in both moduli is evidenced versus applied frequency for the lamellar block copolymer material with and without LiTFSI salt. By virtue of the decoupling of this electrolyte's conductive and mechanical properties, therefore, an exciting new field of electrochemistry was opened. The possibility of a high-energy metallic lithium battery based on this nanostructured solid electrolyte motivates the work detailed herein.

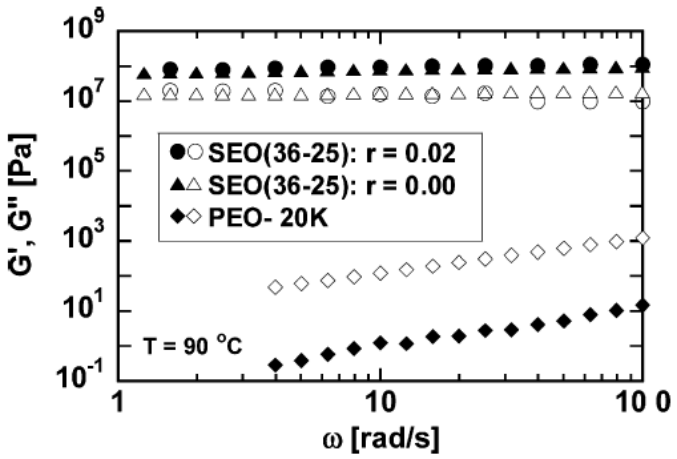

Figure 1.9. Rheological measurements on PS-b-PEO with and without salt compared to homopolymer PEO.[55] The storage modulus (filled symbols) and loss modulus (hollow symbols) demonstrate the advantage of the block copolymer electrolyte over the homopolymer system in terms of mechanical strength. Figure is reproduced from Reference 55.

In the following chapters, the detailed characterization of the PS-b-PEO block copolymer electrolyte system is described. In Chapter 2, I investigate fundamental ionic transport of a lithium salt through this material. Measurements include the ionic conductivity, diffusion coefficient, and transference number for a wide range of LiTFSI salt concentrations at 80 °C, representing a complete set of transport properties directly applicable to first-principles theoretical modeling based on concentrated solution theory. In Chapter 3 the fabrication of block copolymer-based Li/$LiFePO_4$ cells is detailed, for direct comparison with more conventional homopolymer-electrolyte batteries made from PEO. Therein, I perform an in-depth electrochemical characterization on cells containing each electrolyte, cycled as many as 1000 times, to understand the exceptional thermal and electrochemical stability demonstrated by the block copolymer system. Furthermore, electron microscopic evidence of dendrite resistance is shown, and outstanding capacity retention, electrolyte stability, and coulombic and energetic efficiency is documented for that system. Finally, in Chapter 4, I describe the in-situ measurements via synchrotron x-ray spectroscopic techniques we have made to probe the internal electrochemistry of the nanostructured solid electrolyte, measuring for the first time sub-micron-scale salt concentration maps in working lithium batteries. This technique has the potential to provide a wealth of experimental data for corroborating fundamental measurements like those reported in Chapter 2. Furthermore, via these seminal experiments, we demonstrate the measurement of lithium transference in PS-b-PEO and describe a powerful general technique for future, *in situ* fundamental studies on this and other electrochemical systems.

1.2. References

1 Cairns, E. J. and Albertus, P. in *Annual Review of Chemical and Biomolecular Engineering, Vol 1.* 299-320 (Annual Reviews, 2010).

2 Ozawa, K. Lithium-ion rechargeable batteries with $LiCoO_2$ and carbon electrodes - The $LiCoO_2$ carbon system. *Solid State Ionics* **69**, 212-221 (1994).

3 Newman, J. and Tiedemann, W. Simulation of recombinant lead-acid batteries. *Journal of the Electrochemical Society* **144**, 3081-3091 (1997).

4 Ovshinsky, S. R., Fetcenko, M. A. and Ross, J. A nickel metal hydride battery for electric vehicles. *Science* **260**, 176-181 (1993).

5 Paxton, B. and Newman, J. Modeling of nickel/metal hydride batteries. *Journal of the Electrochemical Society* **144**, 3818-3831 (1997).

6 Fetcenko, M. A. *et al.* Recent advances in NiMH battery technology. *Journal of Power Sources* **165**, 544-551 (2007).

7 Howard, W. F. and Spotnitz, R. M. Theoretical evaluation of high-energy lithium metal phosphate cathode materials in Li-ion batteries. *Journal of Power Sources* **165**, 887-891 (2007).

8 Tarascon, J. M. and Armand, M. Issues and challenges facing rechargeable lithium batteries. *Nature* **414**, 359-367 (2001).

9 Bates, J. B., Dudney, N. J., Neudecker, B., Ueda, A. and Evans, C. D. Thin-film lithium and lithium-ion batteries. *Solid State Ionics* **135**, 33-45 (2000).

10 Meyer, W. H. Polymer electrolytes for lithium-ion batteries. *Advanced Materials* **10**, 439 (1998).

11 Croce, F., Appetecchi, G. B., Persi, L. and Scrosati, B. Nanocomposite polymer electrolytes for lithium batteries. *Nature* **394**, 456-458 (1998).

12 Abraham, K. M. Directions in secondary lithium battery research-and-development. *Electrochimica Acta* **38**, 1233-1248 (1993).

13 Ohzuku, T. and Makimura, Y. Layered lithium insertion material of $LiNi_{1/2}Mn_{1/2}O_2$: A possible alternative to LiCoO2 for advanced lithium-ion batteries. *Chemistry Letters*, 744-745 (2001).

14 Koksbang, R., Barker, J., Shi, H. and Saidi, M. Y. Cathode materials for lithium rocking chair batteries. *Solid State Ionics* **84**, 1-21 (1996).

15 Spahr, M. E., Novak, P., Schnyder, B., Haas, O. and Nesper, R. Characterization of layered lithium nickel manganese oxides synthesized by a novel oxidative coprecipitation method and their electrochemical performance as lithium insertion electrode materials. *Journal of the Electrochemical Society* **145**, 1113-1121 (1998).

16 Liu, W., Farrington, G. C., Chaput, F. and Dunn, B. Synthesis and electrochemical studies of spinel phase LiMn2O4 cathode materials prepared by the Pechini process. *Journal of the Electrochemical Society* **143**, 879-884 (1996).

17 Takahashi, M., Tobishima, S., Takei, K. and Sakurai, Y. Characterization of $LiFePO_4$ as the cathode material for rechargeable lithium batteries. *Journal of Power Sources* **97-8**, 508-511 (2001).

18 Whittingham, M. S., Song, Y. N., Lutta, S., Zavalij, P. Y. and Chernova, N. A. Some transition metal (oxy)phosphates and vanadium oxides for lithium batteries. *Journal of Materials Chemistry* **15**, 3362-3379 (2005).
19 Padhi, A. K., Nanjundaswamy, K. S. and Goodenough, J. B. Phospho-olivines as positive-electrode materials for rechargeable lithium batteries. *Journal of the Electrochemical Society* **144**, 1188-1194 (1997).
20 Yang, S. F., Song, Y. N., Zavalij, P. Y. and Whittingham, M. S. Reactivity, stability and electrochemical behavior of lithium iron phosphates. *Electrochemistry Communications* **4**, 239-244 (2002).
21 Srinivasan, V. and Newman, J. Discharge model for the lithium iron-phosphate electrode. *Journal of the Electrochemical Society* **151**, A1517-A1529 (2004).
22 Xing, L. D. *et al.* Theoretical Investigations on Oxidative Stability of Solvents and Oxidative Decomposition Mechanism of Ethylene Carbonate for Lithium Ion Battery Use. *Journal of Physical Chemistry B* **113**, 16596-16602 (2009).
23 Xu, K. Nonaqueous liquid electrolytes for lithium-based rechargeable batteries. *Chemical Reviews* **104**, 4303-4417 (2004).
24 Gnanaraj, J. S., Zinigrad, E., Levi, M. D., Aurbach, D. and Schmidt, M. A comparison among $LiPF_6$, $LiPF_3(CF_2CF_3)_{(3)}$ (LiFAP), and $LiN(SO_2CF_2CF_3)_{(2)}$ (LiBETI) solutions: electrochemical and thermal studies. *Journal of Power Sources* **119**, 799-804 (2003).
25 Aurbach, D., Zinigrad, E., Cohen, Y. and Teller, H. A short review of failure mechanisms of lithium metal and lithiated graphite anodes in liquid electrolyte solutions. *Solid State Ionics* **148**, 405-416 (2002).
26 Arora, P., White, R. E. and Doyle, M. Capacity fade mechanisms and side reactions in lithium-ion batteries. *Journal of the Electrochemical Society* **145**, 3647-3667 (1998).
27 Choi, S. S. and Lim, H. S. Factors that affect cycle-life and possible degradation mechanisms of a Li-ion cell based on LiCoO2. *Journal of Power Sources* **111**, 130-136 (2002).
28 Kanevskii, L. S. and Dubasova, V. S. Degradation of lithium-ion batteries and how to fight it: A review. *Russian Journal of Electrochemistry* **41**, 1-16 (2005).
29 Zhang, D. *et al.* Studies on capacity fade of lithium-ion batteries. *Journal of Power Sources* **91**, 122-129 (2000).
30 Scrosati, B. Battery technology - challenge of portable power. *Nature* **373**, 557-558 (1995).
31 Aurbach, D., Zinigrad, E., Teller, H. and Dan, P. Factors which limit the cycle life of rechargeable lithium (metal) batteries. *Journal of the Electrochemical Society* **147**, 1274-1279 (2000).
32 Bhattacharyya, R. *et al.* In situ NMR observation of the formation of metallic lithium microstructures in lithium batteries. *Nature Materials* **9**, 504-510 (2010).
33 Crowther, O. and West, A. C. Effect of electrolyte composition on lithium dendrite growth. *Journal of the Electrochemical Society* **155**, A806-A811 (2008).
34 Nishikawa, K. *et al.* In Situ Observation of Dendrite Growth of Electrodeposited Li Metal. *Journal of the Electrochemical Society* **157**, A1212-A1217 (2010).
35 Orsini, F. *et al.* In situ Scanning Electron Microscopy (SEM) observation of interfaces within plastic lithium batteries. *Journal of Power Sources* **76**, 19-29 (1998).

36 Mandal, B. K., Padhi, A. K., Shi, Z., Chakraborty, S. and Filler, R. Thermal runaway inhibitors for lithium battery electrolytes. *Journal of Power Sources* **161**, 1341-1345 (2006).
37 Monroe, C. and Newman, J. The effect of interfacial deformation on electrodeposition kinetics. *Journal of the Electrochemical Society* **151**, A880-A886 (2004).
38 Monroe, C. and Newman, J. Dendrite growth in lithium/polymer systems - A propagation model for liquid electrolytes under galvanostatic conditions. *Journal of the Electrochemical Society* **150**, A1377-A1384 (2003).
39 Han, Y. K., Lee, S. U., Ok, J. H., Cho, J. J. and Kim, H. J. Theoretical studies of the solvent decomposition by lithium atoms in lithium-ion battery electrolyte. *Chemical Physics Letters* **360**, 359-366 (2002).
40 Bloom, I. *et al.* An accelerated calendar and cycle life study of Li-ion cells. *Journal of Power Sources* **101**, 238-247 (2001).
41 Fan, J. and Tan, S. Studies on charging lithium-ion cells at low temperatures. *Journal of the Electrochemical Society* **153**, A1081-A1092 (2006).
42 Baril, D., Michot, C. and Armand, M. Electrochemistry of liquids vs. solids: Polymer electrolytes. *Solid State Ionics* **94**, 35-47 (1997).
43 Abraham, K. M., Jiang, Z. and Carroll, B. Highly conductive PEO-like polymer electrolytes. *Chemistry of Materials* **9**, 1978-1988 (1997).
44 Fan, L. Z., Dang, Z. M., Nan, C. W. and Li, M. Thermal, electrical and mechanical properties of plasticized polymer electrolytes based on PEO/P(VDF-HFP) blends. *Electrochimica Acta* **48**, 205-209 (2002).
45 Gorecki, W., Jeannin, M., Belorizky, E., Roux, C. and Armand, M. Physical-properties of solid polymer electrolyte PEO(LiTFSI) complexes. *Journal of Physics-Condensed Matter* **7**, 6823-6832 (1995).
46 Quartarone, E., Mustarelli, P. and Magistris, A. PEO-based composite polymer electrolytes. *Solid State Ionics* **110**, 1-14 (1998).
47 Berthier, C. *et al.* Microscopic investigation of ionic-conductivity in alkali-metal salts poly (ethylene oxide) adducts. *Solid State Ionics* **11**, 91-95 (1983).
48 Lascaud, S. *et al.* Phase-diagrams and conductivity behavior of poly(ethylene oxide) molten-salt rubbery electrolytes. *Macromolecules* **27**, 7469-7477 (1994).
49 Mogi, R. *et al.* Effects of some organic additives on lithium deposition in propylene carbonate. *Journal of the Electrochemical Society* **149**, A1578-A1583 (2002).
50 Shiraishi, S., Kanamura, K. and Takehara, Z. Effect of surface modification using various acids on electrodeposition of lithium. *Journal of Applied Electrochemistry* **25**, 584-591 (1995).
51 Shin, J. H., Henderson, W. A. and Passerini, S. PEO-based polymer electrolytes with ionic liquids and their use in lithium metal-polymer electrolyte batteries. *Journal of the Electrochemical Society* **152**, A978-A983 (2005).
52 Galinski, M., Lewandowski, A. and Stepniak, I. Ionic liquids as electrolytes. *Electrochimica Acta* **51**, 5567-5580 (2006).
53 Monroe, C. and Newman, J. The impact of elastic deformation on deposition kinetics at lithium/polymer interfaces. *Journal of the Electrochemical Society* **152**, A396-A404 (2005).

54 Chadwick, A. V., Strange, J. H. and Worboys, M. R. Ionic transport in polyether electrolytes. *Solid State Ionics* **9-10**, 1155-1160 (1983).
55 Singh, M. *et al.* Effect of molecular weight on the mechanical and electrical properties of block copolymer electrolytes. *Macromolecules* **40**, 4578-4585 (2007).

Chapter 2

Fundamental transport measurements on nanostructured PS-b-PEO electrolytes

2.1. Introduction

Future success of high-energy rechargeable batteries, especially in applications requiring large capacity such as electric vehicles, will require substantial improvements in cell safety and cycle life. These improvements rely, above all else, on increased stability between lithium-conducting electrolytes and high-energy electrode materials.[1] Over the last several years, increasing demand for high-energy Li-ion cells has led to the introduction of higher-potential positive electrodes and higher-capacity negative electrodes, with steady energy-density progress tending to reduce cycle life and system stability. For example, typical capacity fade in recent high-energy Li-ion cells has approached 25% or more per 1000 deep discharge cycles; and thermal stability, particularly of high-voltage Ni-based positive electrodes, has caused concern for large-capacity storage systems.[2-7] The difficulty in achieving a lithium-based rechargeable cell with excellent energy density, cycle life, and safety comes about in large part because of instability between high-energy electrode materials, such as Ni-based metal-oxide positive electrodes and graphite-alloy negative electrodes, and conventional organic, liquid electrolytes (alkyl carbonates containing dissolved $LiPF_6$). Oxidation and reduction of liquid electrolytes at electrode surfaces,[8-11] as well as electrode structural instability and dissolution,[12-14] are responsible for resistance growth, irreversible capacity fade, and thermal instability common to nearly all high-energy-density Li-ion batteries.[15-18]

Despite these challenges, high-energy electrodes are still extremely desirable in rechargeable battery systems. Of all negative-electrode materials, lithium metal remains the most desirable, delivering the theoretical maximum gravimetric energy density for a negative electrode. The incorporation of metallic lithium into rechargeable batteries containing existing liquid, gel-polymer, or solid-polymer electrolytes, however, has repeatedly failed due primarily to the formation of dendritic lithium microstructures that develop with cycling.[19-22] Not only do these "mossy" structures present a larger surface area for electrolyte decomposition and resistive solid-electrolyte interphase (SEI) formation, but also they readily grow into filaments that can penetrate the separator layer and cause premature and dangerous cell failure via rapid internal heating. Catastrophic failures due to fire or explosion as well as gradual failures caused by cell resistance have prevented commercial acceptance of rechargeable lithium batteries to date. That being said, because of the potential gains to energy density conferred by the lithium metal negative electrode, the development of lithium-compatible electrolyte materials is still an active area of research.[20,22-25]

One promising approach toward enabling metallic lithium without succumbing to capacity fade and safety concerns is to use a solid electrolyte having good reductive stability and high mechanical strength. Theoretical modeling by Monroe and Newman has shown that an electrolyte shear modulus exceeding twice that of lithium metal could slow if not altogether eliminate dendrites;[24] and, therefore, it has been theorized that a sufficiently hard conductor should improve lithium-metal cycling. One such group of conductors, solid alkoxy polymers, the most common of which is poly(ethylene oxide) (PEO), has long been studied as potential substitutes for low-modulus liquid electrolytes.[26-28] This group of polymeric materials make appealing candidates for Li-based battery electrolytes for a number of reasons: they readily coordinate lithium ions, they have good electrochemical stability at low potentials, and they possess a high modulus in the crystalline state. However, PEO, like many solid electrolytes, has poor ionic conductivity at room temperature due to insufficient Li-ion mobility. This deficiency comes about because Li-ion mobility is highly correlated to the motion of the polymer chains themselves;[27-29] and, as opposed to rubbery polymers, crystalline polymers like PEO are rigid solids at traditionally relevant temperatures (below ca. 65 °C). While ionic conductivity in the molten state is often orders of magnitude greater than that in the crystalline state, heating above the melting transition comes at the expense of electrolyte rigidity, and the resultant softening imparts reduced chemical and mechanical stability to the electrolyte. The fundamental challenge, therefore, is that the electrical and mechanical properties of traditional polymer electrolytes, including PEO, are coupled: improving conductivity to increase power performance typically leads to faster lithium-electrode surface roughening and thus greater cell instability and quicker cell death.

To address this issue, Singh *et al.* demonstrated in 2007 that a self-assembled block-copolymer, composed of nanoscale conducting channels in a hard polymer matrix, could yield an electrolyte material with high ion-mobility but rigid, glassy bulk properties.[30] It was found that a symmetric block copolymer of polystyrene and polyethylene oxide (PS-b-PEO) achieves sufficient ionic conductivity ($> 10^{-4}$ S/cm) for reasonable battery power while maintaining an electrolyte storage modulus ($> 10^{8}$ Pa) more than three orders of magnitude greater than a comparable homopolymer-PEO electrolyte. With this breakthrough, a lithium-metal rechargeable cell with practical power-output and excellent cycle-life could be envisioned.

To date, however, ionic transport in hard-soft, nanostructured block copolymers remains a nascent field with little known about the power performance of practical lithium metal batteries incorporating these materials. Seminal work by Balsara and coworkers has reported the unexpected result that ionic conductivity of the block copolymer electrolyte PS-b-PEO containing LiTFSI actually increases with polymer molecular weight, as opposed to homopolymer-PEO electrolytes. They found that the block copolymer conductivity divided by the volume fraction of the PEO component approaches the conductivity of homopolymer-PEO only above a threshold polymer molecular weight of about 60 kg/mol.[30,31] It was also reported that this trend may depend to the distribution within nanostructured polymer domains of the conducting salt species. For example, LiTFSI was

determined to reside increasingly in the center of the PEO phase as the polymer molecular weight increases.[32] However, the investigation of fundamental transport in this system remains incomplete. A complete characterization of ionic transport would require, in addition to knowledge of ionic conductivity versus salt concentration for a practical polymer-salt combination, knowledge of the concentration dependence of the salt diffusion coefficient and lithium ion transference number. We have undertaken in this work, in similar fashion to that reported for a sodium salt in PEO by Ma and coworkers[33] and for lithium bis(trifluoromethane)sulfonimide (LiTFSI) in PEO by Edman and coworkers,[34] to record a complete set of transport properties for PS-b-PEO containing LiTFSI at 80°C.

The first of these transport properties, the ionic conductivity, is given for a dilute solution in the absence of concentration gradients by Ohm's law:

$$i = -\kappa \nabla \Phi \tag{2.1}$$

where i is the current density and Φ is the electrical potential. Ionic conductivity dictates the potential loss due to transport of ions in response to a polarization and is related to salt mobility and carrier concentration according to

$$\kappa = F^2 \sum_i {z_i}^2 \mu_i c_i \tag{2.2}$$

where F is Faraday's constant, z is the ionic charge, μ is the ion mobility, and c is the ion concentration. κ, the sum of individual ion conductivities for all charged species, determines the potential drop across an electrolyte in response to an electric field, with higher conductivity tending to reduce overpotential and improve electrolyte performance. While operating conductions in a battery tend to drive the system far from equilibrium such that Ohm's law is no longer directly applicable, the ionic resistivity ($1/\kappa$) nevertheless contributes to the total losses in the system.

In part because of the dependence of κ on c according to equation 2.2, the ionic conductivity within an electrolyte can vary by more than an order of magnitude in operating batteries. This variation is due to detrimental salt concentration gradients that form during polarization, and the source of those gradients – common to all non-single-ion conducting electrolytes – is the mobility of dissociated ions other than the charge-caring cation in the system. In the LiTFSI system, for example, $TFSI^-$ anions are driven by a potential gradient in the opposite direction to Li^+ cations. Cell polarization, therefore, results in a driving force for ion pairs to separate; and although this tendency is counteracted by strong electrostatic attraction between opposite charges, it results in a drag force on the desirable transport of Li^+. The drag force negatively impacts cell performance by way of a concentration overpotential, which during direct current operation, contributes a significant voltage penalty to battery operation. The total potential gradient across an electrolyte solution is given, according to concentrated solution theory,[33] by

$$\nabla\Phi = -\frac{i}{\kappa} + \frac{2RT}{F}\left(1 + \frac{d\ln f_{\pm}}{d\ln c}\right)\left(1 - t_{+}^{0}\right)\nabla\ln c \tag{2.3}$$

where Φ is the electrochemical potential, i is the current density in the electrolyte, κ is the ionic conductivity, $f_{\pm}$ is the salt activity, and t_{+}^{0} is the positive ion transference. When rearranged as follows

$$i = -\kappa\nabla\Phi + \frac{2\kappa RT}{F}\left(1 + \frac{d\ln f_{\pm}}{d\ln c}\right)\left(1 - t_{+}^{0}\right)\nabla\ln c \tag{2.4}$$

equation 2.4 can be understood as the sum of the migration and diffusion contributions to the total current density. The first term, or the migration contribution, comes from Ohm's law (also equation 2.1), and the second term accounts for the contribution from diffusion forces. A detailed explanation of the derivation of equation 2.4 can be found in *Electrochemical Systems* by John Newman and Karen E. Thomas-Alyea.[35] In any case, it can be seen that the smaller the value of t_{+}^{0}, and thus the smaller the relative conductivity of the lithium ion as compared to other charged species in the electrolyte, the larger the potential penalty paid as a result.

The magnitude of the concentration gradient is dictated by the relative mobilities of all charged species, positive and negative, in the electrolyte. Transference is the term given to the fraction of charge carried by a particular species in an electrolyte and quantifies this relative mobility. It is defined precisely only in a solution of uniform composition as the fraction of current carried by a particular ion

$$t_i = \frac{z_i F N_i}{i} \tag{2.5}$$

where N_i is total flux of species i.

Despite its importance,[36] however, transference is a difficult quantity to measure and remains uncertain in many electrolyte systems. Conventional methods of measuring transference, including the potentiostatic polarization method,[37,38] rely on traditional current-voltage measurements, relating cell potential to a salt gradient, and have been shown to rely on invalid assumptions and lack mathematical rigor.[39,40] More precise methods, including measurement by NMR of the individual self-diffusion coefficients of counter-ion pairs[41] or quantification of ion concentrations in polarized cells[42] are experimentally arduous, requiring complex cell architecture, *ex situ* analysis, or special salts. In this work, we utilize a simpler, more experimentally accessible measurement based on quantification of the limiting current in lithium symmetric cells. Herein, the limiting current describes the highest current that can be sustained by oxidation and reduction of lithium ions in an electrochemical system and corresponds to the maximum possible ion gradient. In a cell with two planar electrodes, transference is related to the limiting current and salt diffusion coefficient according to

$$i_l = \frac{2c_b FD}{(1-t_+^0)L} \tag{2.6}$$

where i_l is the limiting current, c_b is the bulk salt concentration, D is the mutual salt diffusion coefficient, and L is the distance between electrodes. According to equation 2.6, in order to find the limiting current, and thus the cation transference, the diffusion coefficient must also be measured experimentally.

The diffusion coefficient, which describes mass transport in response to a concentration gradient, according to

$$N_D = -D\nabla c \tag{2.7}$$

where N_D is the flux of a particular species due to a variation in composition, was measured for this block-copolymer electrolyte by the method of restricted diffusion. This technique, based on indirect measurement of the concentration gradient via cell potential monitoring, is known to provide reliable determination of salt diffusion coefficients,[33,43,44] which, representing the average diffusion coefficient of ion pairs in a given system, are directly applicable to mathematical modeling.

In this work, I report the measurement of a complete set of transport properties for a PS-b-PEO copolymer containing lithium bis(trifluoromethane)sulfonimide. By potentioelectrochemical impedance spectroscopy in lithium symmetric cells, I measure the ionic conductivity versus LiTFSI concentration for a wide range of salt concentrations. For the same concentration range, I measure the LiTFSI diffusion coefficient by the method of restricted diffusion. In order to quantify the relative mobility of the lithium ion to its anionic counterpart, a straightforward method of measuring the lithium transference number is also reported, and I compare the result to a more conventional, but not rigorously defined, method of potentiostatic polarization.

2.2. Experimental

In this work we perform electrochemical measurements on lithium symmetric cells composed of thin lithium foils sandwiching a solid block copolymer electrolyte (BCPE). Lithium was purchased from FMC (100 to 150 μm thickness) and used without modification. The block copolymer electrolyte is poly(styrene-block-ethylene oxide) (55/45 wt/wt%) and was synthesized by anionic polymerization as described previously.[30] LiTFSI was purchased from Ferro and used without purification. To make electrolyte films, LiTFSI was dissolved at the appropriate concentration along with block copolymer in NMP (11 wt% polymer) and cast onto an aluminum substrate using a hand-held doctor blade. Cast films were dried under vacuum at 90 °C for 12 hours and subsequently peeled off the substrate to make free-standing films. Electrolyte film thickness varied between 20 and 55 microns depending on the experiment but was always uniform (within 10% thickness) and without visible defects. Cells for analysis were made by sandwiching two lithium foils of the

same area (defined by punching with steel-rolled dies) on either side of a single, larger-area, free-standing electrolyte (also defined by punching with a steel-rolled die). Polypropylene bags were used to enclose the cells while the electrodes were laminated to the polymer film by pressing at 1000 psi at 90 °C for 5 s. Finally, lithium electrodes were connected to Ni tab material (Pred Materials) via cold-pressing and sealed inside a hermetic, polymer-coated Al pouch (Pred Materials). All cell fabrication steps were performed either in an Argon-filled glovebox (< 1 ppm H_2O) or inside a dryroom (< 0.5% RH).

Electrochemical analysis was performed on a VMP3 impedance analyzer made by Biologic Instruments, interfaced with a PC. All testing was performed on cells heated to 80 °C. Temperature was controlled in forced convection ovens with better than 1 degree temperature precision.

2.3. Results and Discussion

Cells under investigation have the configuration Li/BCPE/Li, as depicted in Figure 2.1. A symmetric cell of this type has zero electrochemical potential difference, and, because both electrodes are solid, planar, and well-characterized, it provides a convenient tool for measuring the electrochemical properties of solid electrolyte materials such as PS-b-PEO containing LiTFSI.

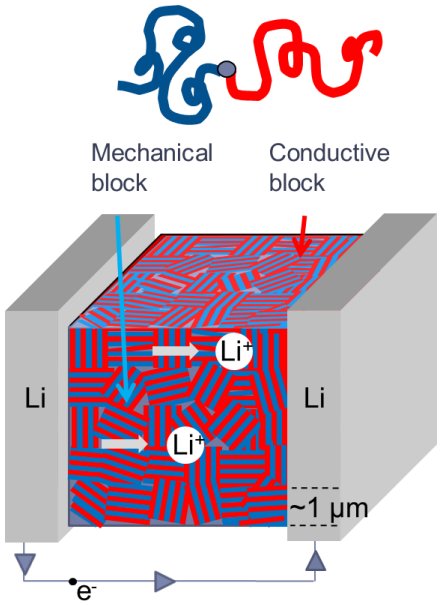

Figure 2.1. Lithium symmetric cell configuration. Three dimensional representation of a lithium symmetric cells shows a graphical depiction of nanosclae grain structure formed by PS-b-PEO block copolymer. Actual domain size is on the order of tens of nanometers with typical grains being approximately 1 micron. A typical electrolyte thickness is 20 to 50 micrometers.

The ionic conductivity of the bulk material is measured by potentioelectrochemical impedance spectroscopy (PEIS). By this method, a frequency sweep of a 25 mV alternating sinusoidal potential is applied between 500 kHz and 100 mHz, in order to quantify the total system impedance (Z) as a function of applied frequency. A typical Nyquist plot, showing the in-phase (real) and out-of-phase (imaginary) components is shown in Figure 2.2. Herein, approximate frequencies are labeled for reference. PEIS allows for the isolation of transport mechanisms in the system with different response times, and it is best interpreted by analyzing the complex impedance data with an equivalent circuit model. The simplest such model that can accurately describe this system is shown in Figure 2.3, incorporating a resistor (the electrolyte) in series with two parallel RC circuits (electrolyte-electrode interfaces), which account for both capacitance and charge transfer resistance at each lithium surface. A Warburg impedance element, describing the solid-state diffusion of lithium ions present at lower frequencies and characterized by a straight line at a 45 degree angle to the x-axis, can be added as shown in Figure 2.3b. In both models, electrical resistance through the leads and electrodes is neglected. In Figure, 2.3c, a representative Nyquist plot depicting the behavior of the equivalent circuit in Figure 2.3b is displayed. It can be seen that the shape of the trace derived from the real Li symmetric cell data (Figure 2.2) matches the graph in Figure 2.3c.

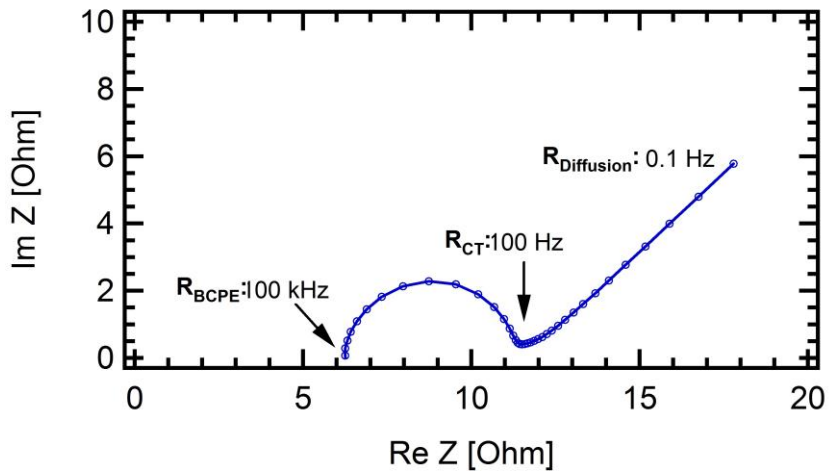

Figure 2.2. Nyquist plot of a representative Li/BCPE/Li cell. A representative plot of the imaginary versus real impedance in a symmetric lithium cell containing a block-copolymer electrolyte shows typical frequencies for bulk resistance (R_{BCPE}), charge transfer resistance (R_{CT}), and the diffusional Warburg impedance ($R_{Diffusion}$).

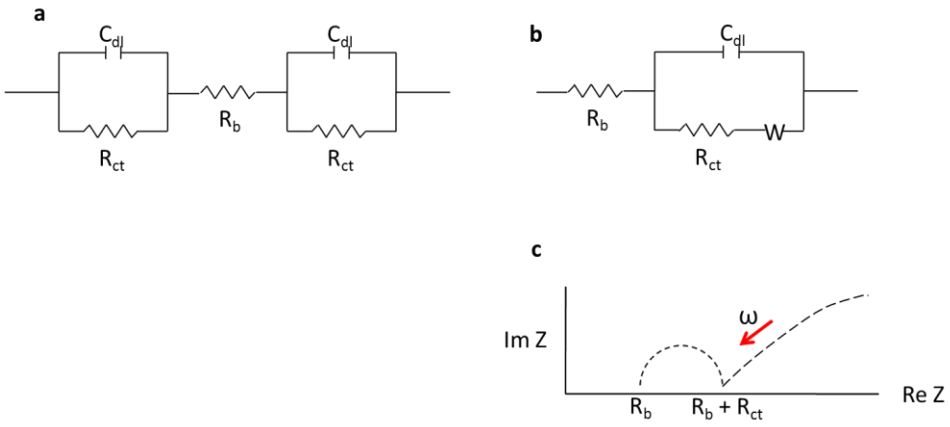

Figure 2.3. Equivalent circuit model of a Li/BCPE/Li cell. a. A simplified equivalent circuit representation of a symmetric lithium cell containing a solid electrolyte shows the various contributions to total resistance: R_b represents the bulk ionic resistance within the solid BCPE, R_{ct} is the charge transfer resistance at each electrolyte-electrode interface, and C_{dl} is the double-layer capacitance at each interface. **b.** A more complete equivalent circuit representation shows a single RC circuit representing the combined interfacial charge transfer and double-layer capacitance as well as the Warburg impedance due to solid-state diffusion of Li ions. **c.** A representative Nyquist complex impedance plot of the equivalent circuit in **b** is depicted along with the relevant resistances, labeled along the x-axis. Resistance decreases with increasing frequency, as depicted.

In the Nyquist plot, the first x-intercept, as determined by a fit to the appropriate equivalent circuit, defines the bulk resistivity of the system. In this system, at frequencies at or above ca. 100 kHz, the response to an applied electric field of dissolved ions within the electrolyte can be isolated. The real impedance at this frequency represents the resistance due to ionic transport through the solid electrolyte but not that due to charge transfer resistance or double layer capacitance, which respond at lower frequencies. It should be noted that because the conductivity of the electrical leads and lithium electrodes exceeds that of the electrolyte by many orders of magnitude (ca. 1 x 10^7 versus ca. 1 x 10^{-4}), electrical impedance can be neglected. As a result, the solid-electrolyte ionic conductivity is calculated according to

$$\kappa = \frac{L}{RA} \tag{2.8}$$

where R is the measured real impedance (ohm) at the first x-intercept, L is the distance between lithium electrodes (cm), and A is the cross-sectional sectional area of the electrodes (cm^2). The BCPE ionic conductivity, measured for a range of LiTFSI salt concentrations, is given in Figure 2.4a, with a maximum value of 2.4 x 10^{-4} S/cm at 80 °C for r = 0.14, where r is defined as the ratio between moles of lithium ions and moles of ethylenoxide units in the polymer chain: [Li]/[EO]. In Figure 2.4b, these results are normalized by LiTFSI molarity, depicting a decrease in the molar conductivity with

increasing salt concentration at 80 °C. Similar to the behavior of homopolymer-PEO containing LiTFSI,[34] this trend in PS-b-PEO can be understood by the effect of increasing LiTFSI content on the transport of Li^+ and $TFSI^-$ in the system. With increasing salt content, cationic motion, which is dependent on polymer segmental motion due to the presence of strong polymer-cation bonds, becomes restricted by an increase in the polymer glass transition temperature; and anionic mobility, dependent on the proximity of free lattice sites large enough for anion occupation, is thought to decrease along with available voids as the electrolyte density increases.[45,46]

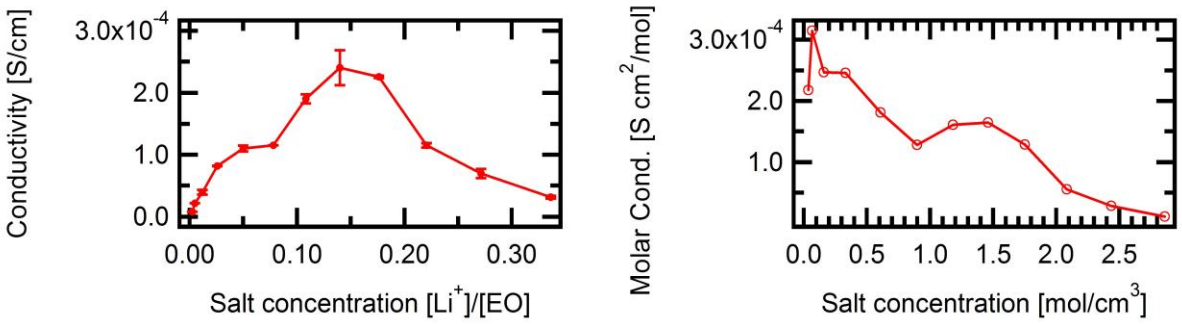

Figure 2.4. Ionic conductivity versus LiTFSI concentration. **a.** The ionic conductivity for PS-b-PEO block copolymer containing various amounts of LiTFSI shows a maximum of 2.4 x 10^{-4} S/cm at 80 °C for r = 0.14, $[Li^+]/[EO]$. Error bars represent one standard deviation. **b.** The molar ionic conductivity for the same salt concentrations is plotted versus salt concentration in mol/cm^3, depicting a decreasing trend with increasing salt content.

The increasing trend of ionic conductivity with salt concentration at low values of LiTFSI is expected according to equation 2.2. By addition of salt to the polymer matrix, an increase in total charge carriers leads to larger total conductivity. However, decreasing molar ionic conductivity (Figure 2.4b) ultimately overwhelms the increase in salt concentration, resulting in a maximum at ca. r = 0.14. In homopolymer-PEO systems a similar increase at low values of LiTFSI has been observed. However, at 80 °C a maximum was reported at r = 0.075, about a factor of two lower than in this block copolymer system.[27] Furthermore, while Panday and coworkers suggest that the optimal salt concentration is r = 0.085 in symmetric PS-b-PEO copolymers containing LiTFSI,[31] in this work, we find that a higher concentration of salt gives up to a factor of two improvement in total ionic conductivity. It should be noted that Panday *et al.* do not report the results on concentrations above r = 0.1, so it is not clear if they would have found a similar increase at even higher salt compositions. Furthermore, the conductivity hump between 0.08 < r < 0.22 seen in Figure 2.4 suggests that a different mechanism may be operating at these concentrations.

In similar Li/BCPE/Li cells, the salt diffusion coefficient was measured by the technique of restricted diffusion. Herein, a constant current density of 0.2 mA/cm^2 is applied between the lithium electrodes for long enough to establish a concentration gradient (varying from

1 to 60 min depending on the cell) but not long enough for the concentration fronts to propagate to the center of the cell, such that the bulk concentration (c_b) remains the same. After polarization, the cell is allowed to return to equilibrium (Figure 2.5a), and during this relaxation period, once double-layer charging has relaxed and potential gradients are allowed to equilibrate, the driving force for salt diffusion is governed by Fick's second law

$$\frac{\partial c}{\partial t} = D\frac{\partial^2 c}{\partial x^2} \tag{2.9}$$

if D is invariant with composition. This restricted diffusion technique has been successfully demonstrated in many systems, including homopolymer-PEO[33,34,43,47,48]. It is known to produce consistent, reliable results because the only forces controlling the movement of ions after a long potential relaxation are diffusional. Furthermore, as the cell approaches equilibrium, a single value of $D(c_b)$ becomes a valid assumption.

During relaxation, close to equilibrium, the natural log of the potential ($\ln \Delta\Phi$) is related to the diffusion coefficient according to[33,48]

$$\ln \Delta\Phi = -\frac{\pi^2 Dt}{L^2} + C \tag{2.10}$$

where C is a constant. At long times, the concentration difference between electrodes is directly related to the potential difference by the Nernst equation, and therefore, cell potential can be used to determine the transients within the cell. As a result, the diffusion of salt due to such a gradient can be readily measured by monitoring the potential over time.

Representative traces of $-\ln \Delta\Phi$ vs t are shown in Figure 2.5b for various polarization times. In these symmetric lithium cells, $\Delta\Phi$ is the measured cell potential, V. As can be seen, the slope of the natural logarithm of the potential relaxation does not change within this range of polarization times, indicating that for this length of time, the proximity of the diffusion fronts to the bulk concentration in the middle of the electrolyte does not affect the measurement. Furthermore, as the traces in Figure 2.5b are linear after ca. 50 s, a linear fit to the data provides accurate determination of $D(c_b)$.

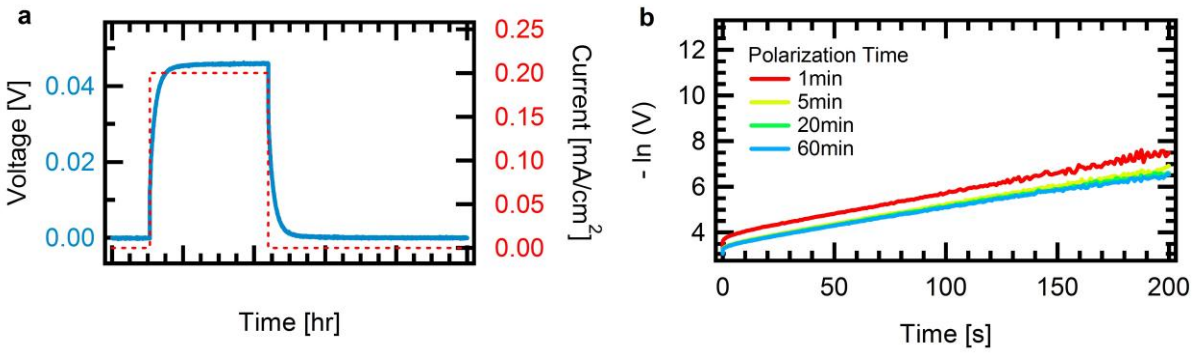

Figure 2.5. Diffusion coefficient measurements by the method of restricted diffusion. a. During relaxation after galvanostatic polarization, salt diffusion is governed by Fick's second law, and potential versus time can be used to calculate the diffusion coefficient in solid electrolyte materials. **b.** –ln (*V*) is plotted versus time during relaxation in order to determine the diffusion coefficient on LiTFSI in the BCPE. Polarization times between 1 and 60 min give the same relaxation behavior.

From the slope of $-\ln \Delta\Phi$ vs t for each LiTFSI concentration, the diffusion coefficient is calculated at 80 °C, as displayed in Figure 2.6, with a maximum of 3.2 x 10^{-8} cm^2/s at r = 0.11. A similar hump between 0.08 < r < 0.22 in the diffusion coefficient and the ionic conductivity gives further evidence for an influence on these properties of the block copolymer microphase structure, not found in homopolymer electrolytes. That being said, the relative independence of the salt diffusion coefficient on LiTFSI concentration, with the maximum and minimum values of D separated by just over a factor of 3, corresponds to results reported for homopolymer-PEO containing both LiTFSI and $LiPF_6$.[34,46] This behavior has been ascribed to the contribution to diffusion of neutral salt pairs, increasingly prevalent at higher salt concentrations.[46]

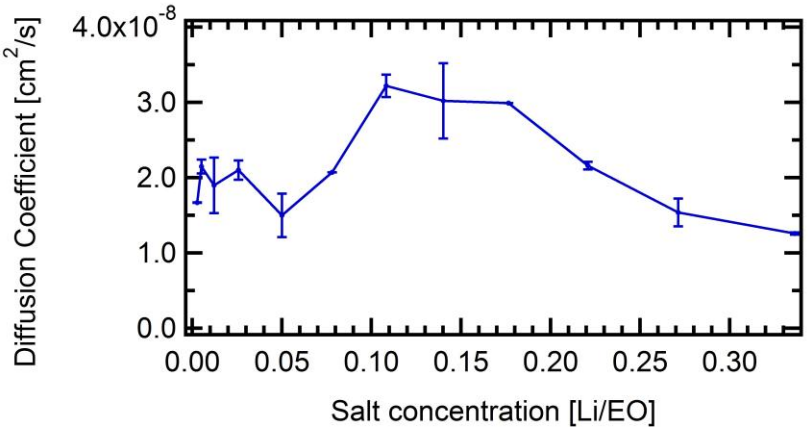

Figure 2.6. **Diffusion coefficient versus LiTFSI concentration**. The salt diffusion coefficient for PS-b-PEO block copolymer containing various amounts of LiTFSI shows a maximum of 3.2 x 10^{-8} cm^2/s at 80 °C for r = 0.11, [Li]/[EO]. Error bars represent one standard deviation.

Lithium transference for a range of LiTFSI concentrations is measured in similar BCPE-containing lithium symmetric cells by galvanostatic polarization at increasing current densities, whereby the limiting current is found. The limiting current represents the maximum current density an electrolyte can sustain before the onset of a rapid, nonlinear increase in potential, which indicates unsustainable depletion of reactants at the cathode surface and a maximum salt concentration gradient. Typical voltage behavior versus time for increasing current densities is depicted in Figure 2.7a, and the resulting log-log plot of voltage, measured at the end of each 30 min polarization, versus applied current density is shown in Figure 2.7b. The normalized cell overpotential versus normalized current density for a range of salt concentrations is depicted in Figure 2.8. The normalization of potential is performed by dividing the measured cell potential by electrolyte thickness in order to standardize for thickness variations among samples. Because the absolute potential is not a factor in equation 2.6, from which the lithium transference is calculated, this normalization assists with visualizing the data but does not affect the calculation.

Similarly, because the limiting current is inversely proportional to electrolyte thickness according to equation 2.6, the current density is normalized according to

$$i_{\mathrm{Norm}} = i\,\frac{L}{20\ \mu m} \tag{2.11}$$

where i is the applied current density and L is the electrolyte thickness in micrometers. This normalization approximates the expected limiting current through an electrolyte in a practical lithium-based battery having a separator thickness of 20 micrometers. In the transference calculation, this normalization also has no effect on the result.

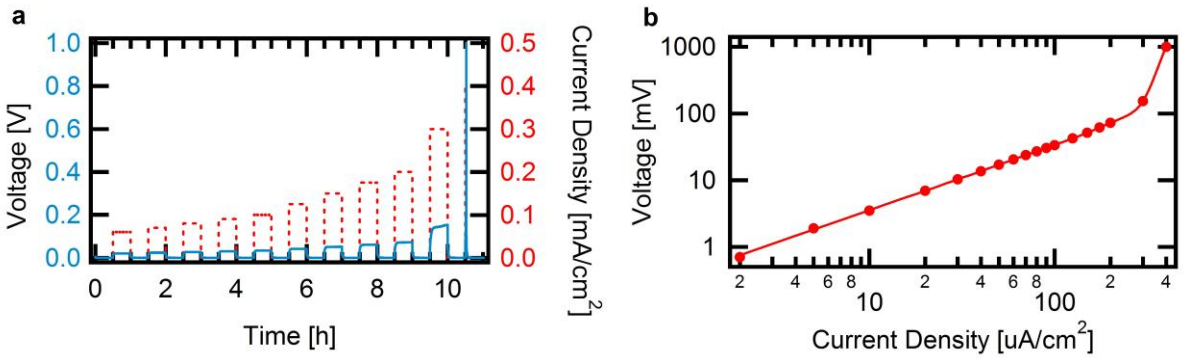

Figure 2.7. Limiting current measured by the galvanostatic polarization method. a. Voltage (solid blue) and current density (dashed red) are plotted versus time for increasing current densities, separated by full rest, ultimately showing nonlinear behavior as the limiting current is reached. **b.** The limiting current, defined as the maximum current sustainable by the solid electrolyte, is indicated by the deviation from linearity in the log-log plot.

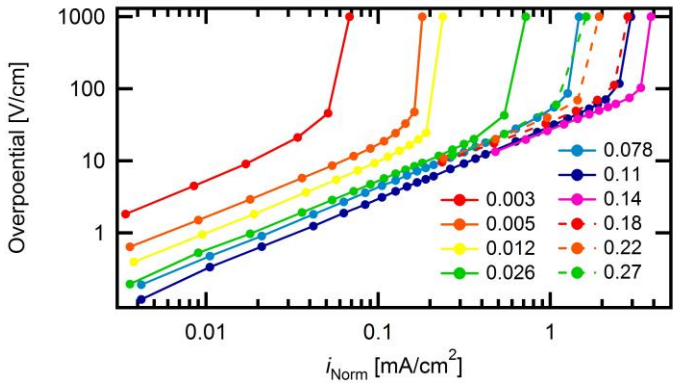

Figure 2.8. Overpotential versus normalized current density for a range of LiTFSI concentrations. The limiting current is found for a range of salt concentrations between r = 0.003 and r = 0.27. For appropriate comparison, overpotential is divided by electrolyte thickness. Because the limiting current is inversely proportional to electrolyte thickness, current density is also normalized by multiplying the applied current density by the ratio of the electrolyte thickness to 20 μm (a typical separator thickness). As salt concentration increases, the limiting current also increases until r = 0.18, at which point salt precipitation and reaction prevent accurate determination.

From the limiting current at each salt concentration, the transference number can be found according to equation 2.6, if the mutual salt diffusion coefficient and the cell geometry are known. A plot of calculated limiting current values (normalized by electrolyte thickness) versus LiTFSI salt concentration is seen in Figure 2.9a, along with the calculated transference number for the same salt concentrations in Figure 2.9b.

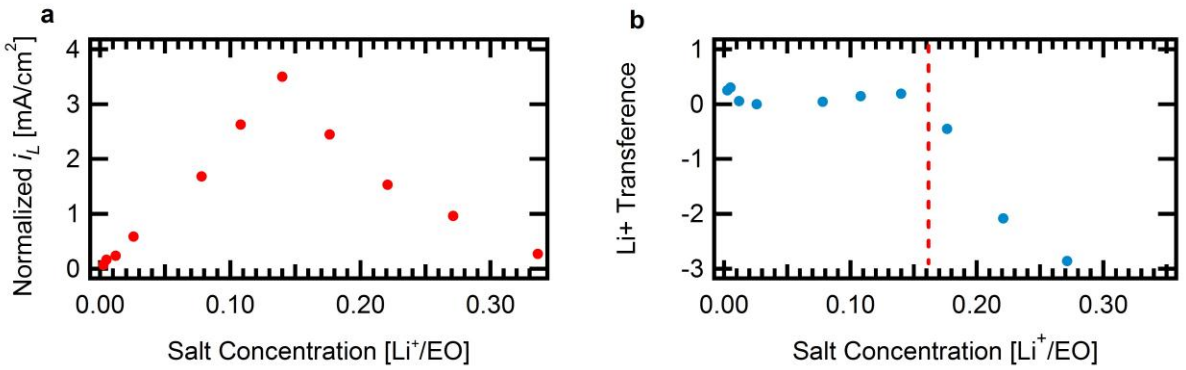

Figure 2.9. Limiting current and lithium transference versus LiTFSI concentration. a. The limiting current (normalized to a 20 μm electrolyte film) in Li/BCPE/Li cells initially increases, as expected, due to an increase in charge carriers. However, above r = 0.14, the measured value decreases, which is attributed to salt precipitation or reaction at the lithium anode. **b.** The lithium transference in Li/BCPE/Li is also found, for a range of salt concentrations. Due to inaccessibility of the limiting current, the dashed line represents the limit of data validity.

At low salt concentrations, the lithium transference shows a slight decrease followed by an increase before r = 0.14. Previous literature reports of Li^+ transference in PEO containing LiTFSI by Edman and coworkers report an increase from about 0.2 to 0.6 over the range of LiTFSI compositions $0.033 < c < 0.2$, measured according to concentrated solution theory via concentration cells.[34] While inconsistent results found by a variety of techniques have been reported in similar systems,[49] herein a relatively constant cation transference indicates that cation and anion mobility are similarly affected by increasing salt concentration.

At higher salt concentrations, above r = 0.14, the limiting current cannot be measured accurately by this technique due to a rapid increase in interfacial resistance during polarization in these systems. This increase is significant and irreversible, which indicates salt reaction and/or precipitation against the lithium anode before the true limiting current is reached. Because the limiting current remains unknown at higher salt values, therefore, the transference number also cannot be calculated by this method above r = 0.14. However, because this range exceeds typical salt quantities found in useful polymer electrolytes (which must, for example, remain electrochemically stable), this limitation is not of practical concern. It should also be noted that because a salt gradient is setup during the limiting current experiment, not one, but a continuous range of diffusion coefficients is operable in the system. Therefore, equation 2.6 relies on integrated diffusion coefficient for accurate calculation of the lithium transference for a given bulk salt concentration, c_b.

For comparison with transference numbers measured by a more common technique,[38] we have also performed potentiostatic polarization on lithium symmetric cells containing the BCPE electrolyte, and we have compared them to the value calculated by our novel

approach. In table 2.1, the results can be seen for a salt concentration of r = 0.11. By the potentiostatic polarization method, the lithium transference can be estimated according to

$$t_+ = \frac{I_S(\Delta V - I_0 R_0)}{I_0(\Delta V - I_S R_S)} \tag{2.12}$$

where the initial (I_0) and steady-state current densities (I_S) are corrected for differences in the initial ($\Delta V - I_0 R_0$) and steady-state ($\Delta V - I_S R_S$) interfacial resistance.

Table 2.1. Lithium transference calculated by two different methods

Method	**Lithium transference at r=0.11 in LiTFSI**
Potentiostatic polarization	0.14
Limiting current	0.15

It is interesting to find such close agreement between the lithium transference measured by these two techniques, as it is known that the method of potentiostatic polarization is not rigorously accurate. However, many previous reports of transference measured by potentiostatic polarization have come very close to those found by more accurate methods, indicating that it is likely a close approximation in most cases.

2.4. Conclusion

A complete set of transport properties in the PS-b-PEO system was measured for the LiTFSI salt. Over a range, 0.003 < r < 0.34, the ionic conductivity, salt diffusion coefficient, and lithium transference number were determined at 80 °C. Values of the ionic conductivity measured in this work are similar to those reported previously for symmetric PS-b-PEO, although a maximum is found at r = 0.14 in this study, higher than previously reported. A decrease of 3 to 5 times the ionic conductivity of homopolymer-PEO is found, which can be explained primarily by the reduced volume of conducting material as well as grain-structure effects present in this microphase separated material. The diffusion coefficient is also reduced by less than an order of magnitude relative to homopolymer-PEO, which can be understood in the same way. Via a straight-forward method of calculating the transference number, we measure the lithium transference in this system at practical salt concentrations, and the results are not inconsistent with reported values for other ethyleneoxide-based solid conductors.

2.5. References

1 Cairns, E. J. and Albertus, P. *Annual Review of Chemical and Biomolecular Engineering, Vol 1.* 299-320 (2010).

2 Takei, K. *et al.* Cycle life estimation of lithium secondary battery by extrapolation method and accelerated aging test. *Journal of Power Sources* **97-8**, 697-701 (2001).

3 Takei, K. *et al.* Performance of large-scale secondary lithium batteries for electric vehicles and home-use load-leveling systems. *Journal of Power Sources* **119**, 887-892, (2003).

4 Choi, S. S. and Lim, H. S. Factors that affect cycle-life and possible degradation mechanisms of a Li-ion cell based on LiCoO2. *Journal of Power Sources* **111**, 130-136 (2002).

5 Gnanaraj, J. S., Zinigrad, E., Levi, M. D., Aurbach, D. and Schmidt, M. A comparison among LiPF6, LiPF3(CF2CF3)(3) (LiFAP), and LiN(SO2CF2CF3)(2) (LiBETI) solutions: electrochemical and thermal studies. *Journal of Power Sources* **119**, 799-804, (2003).

6 Kanevskii, L. S. and Dubasova, V. S. Degradation of lithium-ion batteries and how to fight it: A review. *Russian Journal of Electrochemistry* **41**, 1-16 (2005).

7 Mandal, B. K., Padhi, A. K., Shi, Z., Chakraborty, S. and Filler, R. Thermal runaway inhibitors for lithium battery electrolytes. *Journal of Power Sources* **161**, 1341-1345, (2006).

8 Aurbach, D. Review of selected electrode-solution interactions which determine the performance of Li and Li ion batteries. *Journal of Power Sources* **89**, 206-218 (2000).

9 Edstrom, K., Gustafsson, T. and Thomas, J. O. The cathode-electrolyte interface in the Li-ion battery. *Electrochimica Acta* **50**, 397-403, (2004).

10 Ein-Eli, Y. A new perspective on the formation and structure of the solid electrolyte interface at the graphite anode of Li-ion cells. *Electrochemical and Solid State Letters* **2**, 212-214 (1999).

11 Aurbach, D. *et al.* On the capacity fading of LiCoO2 intercalation electrodes: the effect of cycling, storage, temperature, and surface film forming additives. *Electrochimica Acta* **47**, 4291-4306 (2002).

12 Dokko, K. *et al.* In situ observation of LiNiO2 single-particle fracture during Li-ion extraction and insertion. *Electrochemical and Solid State Letters* **3**, 125-127 (2000).

13 Zhang, X. C., Shyy, W. and Sastry, A. M. Numerical simulation of intercalation-induced stress in Li-ion battery electrode particles. *Journal of the Electrochemical Society* **154**, A910-A916, (2007).

14 Blyr, A. *et al.* Self-discharge of LiMn2O4/C Li-ion cells in their discharged state - Understanding by means of three-electrode measurements. *Journal of the Electrochemical Society* **145**, 194-209 (1998).

15 Arora, P., White, R. E. and Doyle, M. Capacity fade mechanisms and side reactions in lithium-ion batteries. *Journal of the Electrochemical Society* **145**, 3647-3667 (1998).

16 Zhang, D. *et al.* Studies on capacity fade of lithium-ion batteries. *Journal of Power Sources* **91**, 122-129 (2000).

17 Sloop, S. E., Kerr, J. B. and Kinoshita, K. The role of Li-ion battery electrolyte reactivity in performance decline and self-discharge. *Journal of Power Sources* **119**, 330-337, (2003).
18 Vetter, J. *et al.* Ageing mechanisms in lithium-ion batteries. *Journal of Power Sources* **147**, 269-281, (2005).
19 Brissot, C., Rosso, M., Chazalviel, J. N. and Lascaud, S. Dendritic growth mechanisms in lithium/polymer cells. *Journal of Power Sources* **81**, 925-929 (1999).
20 Orsini, F. *et al.* In situ Scanning Electron Microscopy (SEM) observation of interfaces within plastic lithium batteries. *Journal of Power Sources* **76**, 19-29 (1998).
21 Aurbach, D., Zinigrad, E., Teller, H. and Dan, P. Factors which limit the cycle life of rechargeable lithium (metal) batteries. *Journal of the Electrochemical Society* **147**, 1274-1279 (2000).
22 Monroe, C. and Newman, J. Dendrite growth in lithium/polymer systems - A propagation model for liquid electrolytes under galvanostatic conditions. *Journal of the Electrochemical Society* **150**, A1377-A1384, (2003).
23 Monroe, C. and Newman, J. The effect of interfacial deformation on electrodeposition kinetics. *Journal of the Electrochemical Society* **151**, A880-A886, (2004).
24 Monroe, C. and Newman, J. The impact of elastic deformation on deposition kinetics at lithium/polymer interfaces. *Journal of the Electrochemical Society* **152**, A396-A404, (2005).
25 Bhattacharyya, R. *et al.* In situ NMR observation of the formation of metallic lithium microstructures in lithium batteries. *Nature Materials* **9**, 504-510, (2010).
26 Berthier, C. *et al.* Microscopic Investigation of Ionic-conductivity in alkali-metal salts poly(ethylene oxide) adducts. *Solid State Ionics* **11**, 91-95 (1983).
27 Lascaud, S. *et al.* Phase-diagrams and conductivity behavior of poly(ethylene oxide) molten-salt rubbery electrolytes. *Macromolecules* **27**, 7469-7477 (1994).
28 Gorecki, W., Jeannin, M., Belorizky, E., Roux, C. and Armand, M. Physical-properties of sollid polymer electrolyte PEO(LiTFSI) complexes. *Journal of Physics-Condensed Matter* **7**, 6823-6832 (1995).
29 Chadwick, A. V., Strange, J. H. and Worboys, M. R. Ionic transport in polyether electroyltes. *Solid State Ionics* **9-10**, 1155-1160 (1983).
30 Singh, M. *et al.* Effect of molecular weight on the mechanical and electrical properties of block copolymer electrolytes. *Macromolecules* **40**, 4578-4585, (2007).
31 Panday, A. *et al.* Effect of Molecular Weight and Salt Concentration on Conductivity of Block Copolymer Electrolytes. *Macromolecules* **42**, 4632-4637, (2009).
32 Gomez, E. D. *et al.* Effect of Ion Distribution on Conductivity of Block Copolymer Electrolytes. *Nano Letters* **9**, 1212-1216, (2009).
33 Ma, Y. P. *et al.* The measurement of a complete set of transport-properties for a concentrated solid polymer electrolyte solution. *Journal of the Electrochemical Society* **142**, 1859-1868 (1995).
34 Edman, L., Doeff, M. M., Ferry, A., Kerr, J. and De Jonghe, L. C. Transport properties of the solid polymer electrolyte system P(EO)(n)LiTFSI. *Journal of Physical Chemistry B* **104**, 3476-3480 (2000).

35 Newman, J. and Thomas-Alyea, K. E. *Electrochemical Systems*. 3rd edn, 297-311 (2004).
36 Doyle, M., Fuller, T. F. and Newman, J. The importance of the lithium ion transference number in lithium polymer cells. *Electrochimica Acta* **39**, 2073-2081 (1994).
37 Watanabe, M., Rikukawa, M., Sanui, K. and Ogata, N. Evaluation of ionic mobility and transference number in a polymeric solid electrolyte by isothermal transient current method.. *Journal of Applied Physics* **58**, 736-740 (1985).
38 Appetecchi, G. B., Dautzenberg, G. and Scrosati, B. A new class of advanced polymer electrolytes and their relevance in plastic-like, rechargeable lithium batteries. *Journal of the Electrochemical Society* **143**, 6-12 (1996).
39 Doyle, M. and Newman, J. Analysis of transference number measurements based on the potentiostatic polarization of solid polymer electrolytes. *Journal of the Electrochemical Society* **142**, 3465-3468 (1995).
40 Hafezi, H. and Newman, J. Verification and analysis of transference number measurements by the galvanostatic polarization method. *Journal of the Electrochemical Society* **147**, 3036-3042 (2000).
41 Dai, H. L. and Zawodzinski, T. A. Determination of lithium ion transference numbers by electrophoretic nuclear magnetic resonance. *Journal of the Electrochemical Society* **143**, L107-L109 (1996).
42 Bruce, P. G., Hardgrave, M. T. and Vincent, C. A. The determination of trasnference numbers in solid polymer electrolytes using the Hittorf method. *Solid State Ionics* **53**, 1087-1094 (1992).
43 Doeff, M. M., Edman, L., Sloop, S. E., Kerr, J. and De Jonghe, L. C. Transport properties of binary salt polymer electrolytes. *Journal of Power Sources* **89**, 227-231 (2000).
44 Pai, S. J., Bae, Y. C. and Sun, Y. K. Electrochemical properties for solid polymer electrolyte/salt systems in lithium secondary batteries. *Journal of the Electrochemical Society* **152**, A864-A870, (2005).
45 Bruce, P. G. and Gray, F. M. *Solid State Electrochemistry*. 140 (University Press, 1995).
46 Arumugam, S., Shi, J., Tunstall, D. P. and Vincent, C. A. Cation and anion diffusion-coefficients in a solid polymer electrolyte measured by pulsed-field-gradient nuclear-magnetic-resonance. *Journal of Physics-Condensed Matter* **5**, 153-160 (1993).
47 Newman, J. and Chapman, T. W. Restricted diffusion in binary-solutions. *Aiche Journal* **19**, 343-348 (1973).
48 Thompson, S. D. and Newman, J. Differential diffusion-coefficients of sodium polysulfide melts. *Journal of the Electrochemical Society* **136**, 3362-3369 (1989).
49 Fritz, H. P. and Kuhn, A. Comparative determination of effective transport numbers in solid lithium electrolytes. *Journal of Power Sources* **41**, 253-261 (1993).

Chapter 3

Electrochemical characterization of all-solid-state, high specific energy Li/$LiFePO_4$ cells

3.1. Introduction

The Li-ion cell, commercially introduced by Sony in 1991, was a major breakthrough for rechargeable-battery systems.[1] The primary advantage of the Li-ion chemistry was its high energy density, which enabled tremendous growth in consumer electronic devices including camcorders, laptops, and cell-phones.[2] Continued progress into larger-capacity batteries, such as those for electric vehicles, distributed-energy storage, and electrical grid-tied storage, however, will require, among other things, substantial improvement in cycle life, with thousands as opposed to hundreds of cycles needed.[3] Over the last several years, the introduction of higher-energy intercalation electrodes has led to significant improvements in the energy density of Li-ion cells, but this progress has come at the expense of cycle life, with typical capacity fade approaching 25% per 1000 deep discharge cycles.[4-6] Furthermore, at higher temperatures, reached frequently as the result of normal battery resistance, Li-ion cells show even faster performance decline. In Figure 3.1, the cycle life of Sony 18650 Li-ion cells at different temperature can be seen, with dramatic capacity fade evident above 45 °C.[7,8] While temperature control can be managed with costly, heavy, and sophisticated cooling systems, poor performance at elevated temperatures poses a significant obstacle to widespread adoption of large-capacity lithium-ion battery systems. With new high-energy electrode materials – Ni-based metal-oxide positive electrodes and graphite or graphite-alloy negative electrodes – finding more frequent use, calendar and cycle life, particularly at elevated temperatures, remain the biggest challenges to electrification of automobiles as well as large-scale energy-backup systems.[9-11]

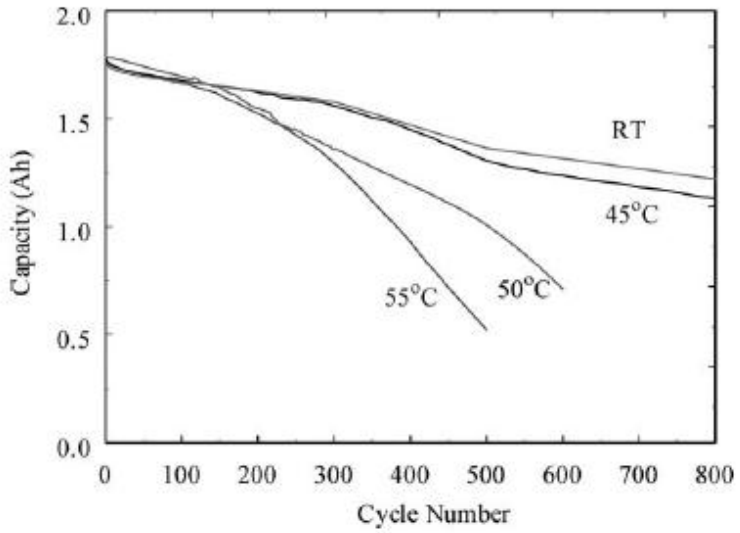

Figure 3.1. Capacity versus cycle number for a Sony Li-Ion cell.[7] The capacity fade of Sony 18650 Li-Ion batteries is compared versus cycle number for a range of temperatures, showing dramatic increase at temperatures above 45°C. Figure reproduced from Reference 7.

Despite these challenges, high-energy rechargeable batteries are attracting ever-more interest inside and outside of academia. It is apparent that their ultimate success – including long calendar and cycle life – requires significant advances in electrode-electrolyte stability, this being one of the primary causes of capacity fade over time and cycling for most lithium-based electrochemical systems.[9,12] For lithium metal, always the holy grail of negative electrodes, success depends on improving the poorly-behaved plating behavior common to all previous electrolytes, including organic liquids, ionic liquids, as well as solid-polymer conductors, used with this aggressive electrode. Despite much effort, rapid formation of dendritic microstructures that develop with cycling has doomed each of these systems in work spanning several decades.[13-16] That being said, theoretical[17-19] and experimental[15,20,21] research on lithium metal continues at a rapid pace, with the development of lithium-compatible electrolyte materials a worthy, albeit challenging goal.

In this work, we demonstrate the incorporation of the hard-soft, block copolymer electrolyte (BCPE), poly(styrene-block-ethylene oxide) (PS-b-PEO) containing lithium bis(trifluoromethane)sulfonimide (LiTFSI), into metallic-lithium batteries to assess its effect on lithium metal cycleability. In particular, we fabricate practical BCPE cells for direct comparison with a model homopolymer-electrolyte (HPE) system composed of poly(ethylene oxide) (PEO) and LiTFSI. Each solid-state system under investigation is composed of a thin metallic-lithium negative electrode and a porous-composite positive electrode made up of lithium iron phosphate ($LiFePO_4$), conductive carbon, and PS-b-PEO electrolyte, with no additional polymeric binder or liquid additive. A graphical

representation of the structure is illustrated in Figure 3.2, with approximate component thicknesses indicated in comparison to a conventional Li-ion cell.

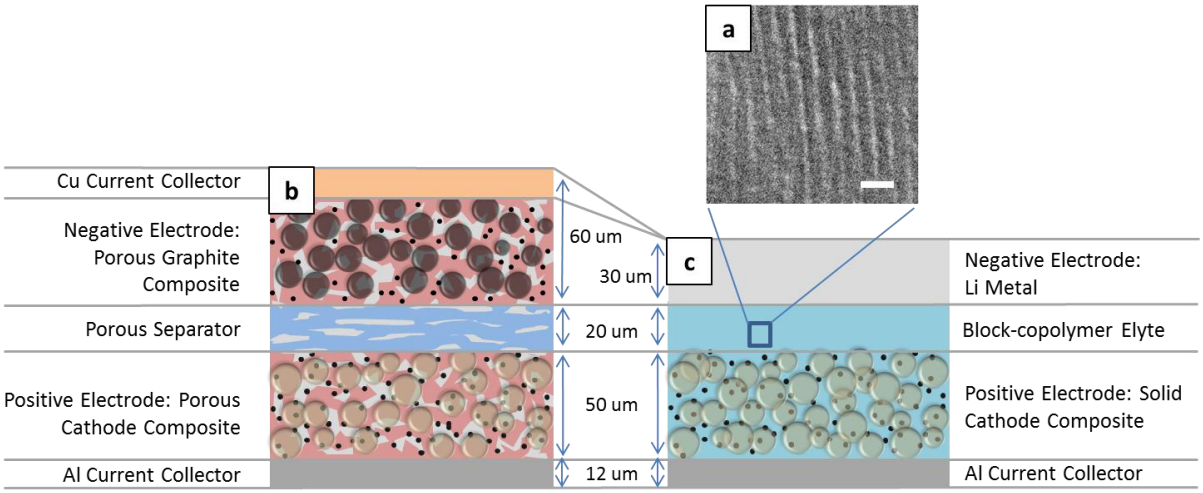

Figure 3.2. Cell configurations of a conventional Li-Ion cell and the all-solid-state lithium metal cell under investigation. a. A transmission electron micrograph shows lamellar, microphase separation between PS and PEO blocks. **b**. The dual-intercalation Li-Ion system is configured from positive and negative porous electrodes, each attached to a current collector and separated by a porous-insulating film containing an organic liquid electrolyte. **c.** The solid-state cell used in this work is composed of a solid lithium anode, a solid BCPE, and a solid cathode, which contains $LiFePO_4$, conductive additive, and BCPE (acting as binder and ion-conducting material). Dimensions are intended as estimates for visualization purposes.

As can be seen, the overall volume of the solid-state lithium metal batteries fabricated for this work is lower than that of a comparable Li-ion cell. In Table 3.1 the approximate masses, scaled to cathode active material, of the cell components required in the practical $Li/LiFePO_4$ system are also compared to a conventional $C_6/LiCoO_2$ system (of the same capacity). Therein, the gravimetric energy advantage of this chemistry can also be compared, with the primary advantages of the former system arising from the high specific capacity of lithium metal compared to a graphite anode (3862 mAh/g versus 372 mAh/g) along with the elimination of a heavy copper current collector required by the latter.

Table 3.1. Mass Comparison of two battery chemistries

	$C_6/LiCoO_2$	$Li/LiFePO_4$
Anode Active	0.51	0.14
Anode Non-Active	0.06	0
Anode Current Collector	1.02	0
Separator/Electrolyte	0.32	0.38
Cathode Active	1	1
Cathode Non-Active	0.19	0.32
Cathode Current Collector	0.33	0.32
Total	**3.42**	**2.16**

Table 3.1. Relative masses of the primary constituents of a practical battery (discounting packaging, tabs, etc.) demonstrate the advantage of the solid-state $Li/LiFePO_4$ system over the conventional, liquid-based $C_6/LiCoO_2$ system. Values are intended as useful approximations and account for excess anode capacity in each system (1.1x for C_6 and 3.0x for Li).

Via many months of cycling at elevated temperature, we demonstrate the advantages of the nanostructured, block copolymer electrolyte in a practical, high-specific-energy, rechargeable battery system. HPE and BCPE cells, repeatedly charged and discharged, are compared according to capacity retention, cell resistance, and efficiency over time and cycling; and the nanostructured electrolyte confers dramatic improvement over the homopolymer electrolyte in all respects. In fact, the BCPE-system displays unprecedented stability, including 1000 deep-discharge cycles with a capacity-retention better than 99.995% per cycle, better to our knowledge than any other high-specific-energy rechargeable battery. Furthermore, by post-mortem scanning electron microscopy (SEM), we show that even after hundreds of cycles, the hard-BCPE prevents lithium dendrite formation, retaining a consistent, uniform lithium-solid-electrolyte interface throughout the cell, as compared to an as-built battery.

3.2. Experimental

Cells for electrochemical analysis are fabricated from the same materials. $LiFePO_4$ was purchased from Phostech Lithium (P2, D50 0.5-0.9 μm) and dried under vacuum along with denka black (Denka Co.) at 150 °C for 8 h. Li foil (30 to 50 μm thick) was purchased from Chemetall or FMC Lithium and used without modification. LiTFSI was purchased from Ferro and used as received. PS-b-PEO was synthesized by anionic polymerization (PEO:PS wt%/wt% 55:45) as described previously.[21] PEO (MW 200 kDa) was used as received. Before use, each polymer material was dried under vacuum at 60 °C for 8 h. BCPE cells contain PS-b-PEO with LiTFSI (2 M in the conducting phase) as the separator and as the electrolyte in the cathode. HPE cells contain PEO with LiTFSI (2 M) as the separator and the BCPE in the cathode.

The composite cathodes for all cells (HPE and BCPE) are composed of $LiFePO_4$, denka black, and polymer electrolyte with similar composition to previous reports for polymer-composite cathodes.[22] Cathode slurries were sonicated and homogenized in cyclohexanone to disperse solid particles and break-up agglomerates, according to published procedures,[23] and subsequently cast onto an aluminum foil current collector using a Hohsen comma-bar coater. The dry laminates were calendered with an Innovative Machine Co. mill to reduced inherent porosity. The cathode-composite mass-loading is approximately 7 mg/cm^2. The separator electrolytes are also cast from cyclohexanone directly onto cathode laminates using the same coating machine. The thickness of each dry separator film is between 20 and 24 microns. The dual-layer film was dried under vacuum at 90 °C for 8 h. The final cell was made by laminating lithium directly to the solid electrolyte by heating to 100 °C for 5 s in a mechanical press. External leads to the electrodes were made with nickel (negative) and aluminum (positive) tab-extensions. Aluminum extensions were sonically welded outside the active area of the cathode to a bare region of the aluminum current collector. Nickel extensions were hot pressed to a lithium extension, also outside the active area of the cell. Final cells were sealed inside a polypropylene-coated aluminum pouch under vacuum, with lead extensions wrapped in heat-sealable plastic strips to ensure a hermetic seal. All cell-fabrication steps were performed in a dry room (<0.5% RH).

DC electrochemical measurements were performed on Arbin BT2000 battery cyclers interfaced with a PC. Current, voltage, capacity, and energy were collected and/or calculated by MITSPro Data Processing software. Efficiency was calculated directly from capacity and energy data. Resistance was calculated as described in the text. Post-mortem sectioning and SEM analysis were performed by Hydro-Québec. Cells for imaging analysis were cycled just as cells for electrochemical analysis.

3.3. Results and Discussion

The electrochemical stability of this novel BCPE system was assessed in several ways. Electrochemical measurements were compared to a comparable system (with identical electrodes) containing a homopolymer electrolyte (HPE) composed of PEO and LiTFSI as the separator. First, batteries with the configuration illustrated in Figure 3.2c, were charged and discharged at a constant C-rate for many months at elevated temperature (80 °C) without rest. C-rate is defined as

$$I/C \tag{3.1}$$

where I is absolute current (A) and C is the total capacity of the cell (Ah). These rates were chosen to approximate a typical average current-draw for an EV application, which requires both high specific energy and long cycle life. Testing was performed at 80 °C to achieve sufficient conductivity for the specified rates and to assess the chemical and electrochemical stability of the system at elevated temperature.[23-27] As conventional Li-ion

cells show a characteristic thermal instability above ca. 45 °C, manifested as loss of capacity and, when not carefully managed, thermal runaway and cell failure, improved performance at elevated temperature is a particularly important advancement.

In Figure 3.3, the specific capacity versus cycle number is shown for three cells: Cell A, containing a PS-b-PEO electrolyte, charged and discharged at a C/2 rate for 1000 full depth-of-discharge (DOD) cycles; Cell B, also containing a PS-b-PEO electrolyte but cycled less-aggressively at half the rate (C/4) to only 80%-DOD; and Cell C, containing a PEO electrolyte, cycled exactly as Cell A. Herein, DOD is defined relative to a cell's maximum capacity utilization for a given rate between voltage cut-off limits and is lower than the theoretical specific capacity (170 mAh/g for $LiFePO_4$). The measured specific capacity ranges from 149 mAh/g (Cell C) to 158 mAh/g (Cell A), or 88 to 93% of the theoretical value (normalized by weight of $LiFePO_4$), which is consistent with previous reports for $LiFePO_4$ in liquid-electrolyte systems and does not vary significantly between HPE or BCPE cells. For Cell B, limited-DOD cycling, which is defined relative to the practical capacity, was accomplished with a coulomb cut-off on charge and employed to assess a strategy to maximize cycle life by avoiding voltage extremes, a common protocol used in electric and hybrid-electric vehicles. For this cell, the lower charging and discharging rates results in decreased cell overpotential, which reduces exposure to high cell voltage as compared to Cell A and Cell C.

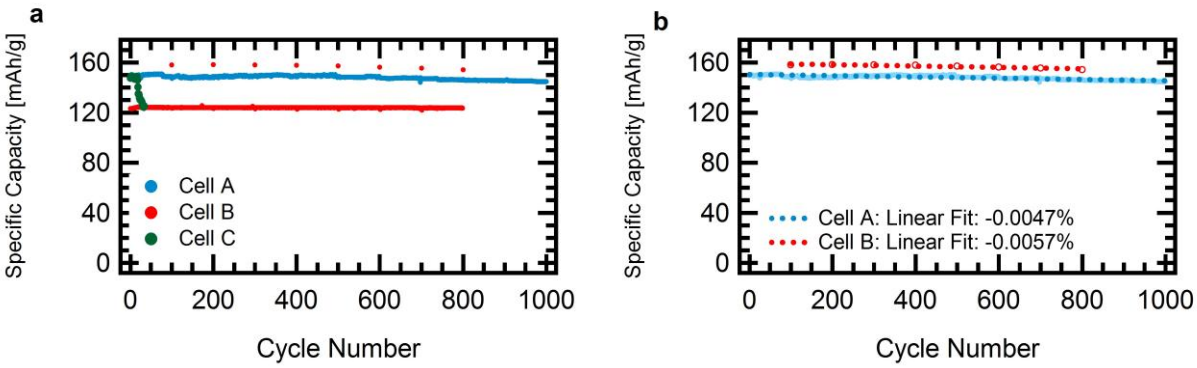

Figure 3.3. **Specific capacity versus cycle number for BCPE and HPE cells**. **a.** The specific capacity (normalized by active material weight in the cathode) declines by only 4.7% after 1000 cycles for Cell A (BCPE electrolyte, cycled full-DOD at C/2). Cell B (BCPE electrolyte, cycled at C/4 to 80%-DOD) shows no fade after 800 cycles. Cell C (HPE electrolyte, cycled full-DOD at C/2) loses 15.2% capacity after 34 cycles. **b.** The C/10, full-DOD discharge cycles for Cell B (once every 100 cycles) are compared to the C/2, full-DOD discharge cycles for Cell A, and a linear fit shows a fade-rate differing by only 0.001% per cycle.

At a C/2 rate, one complete cycle takes ca. 4 h (2 h charge plus 2 h discharge); and, therefore, one thousand cycles represents ca. 4000 h of continuous electrochemical oxidation and reduction. Over this cycling time, an average capacity fade of 0.005% per

cycle and 0.001% per hour (ca. 3937 h) was measured for Cell A. The fade was calculated by the slope of a linear fit to the data (Figure 3.3b), which does an adequate job of approximating the average capacity fade without undue complexity. Discharge capacity versus cycle number for Cell B is also shown in Figure 3.3b. Capacity on discharge for this cell remains constant over 800 cycles, which suggests that coulombic efficiency is excellent but does not give a direct measurement of capacity-fade. For a better comparison of the capacity-fade between limited- and full-DOD cycling, once every 100 cycles, Cell B was also charged and discharged the full-DOD range at C/10, allowing its total available capacity to be quantified on a periodic basis. Comparing the eight full-DOD discharges, Cell B shows a total capacity fade of 4.56% after 800 cycles, or an average of 0.006% per cycle and 0.001% per hour (ca. 5310 h), representing a higher fade rate on a per cycle basis than Cell A but very similar fade on a per time basis. While we expect both time and cycle number to play a role in capacity fade, Cells A and B both show exceptional electrochemical stability with small differences likely caused by cell-to-cell variations in electrodes. In contrast to the BCPE cells, Cell C shows much higher capacity fade. A linear fit is not instructive, as the loss of capacity begins slowly and accelerates after cycle 15 (Figure 3.3a), but the total capacity fade after 34 cycles is 15.2%, which represents an average fade of 0.45% per cycle, more than 75 times higher than that for either BCPE cell.

Voltage versus specific capacity profiles for ten full-DOD cycles, spaced 100 cycles apart, for Cell A are shown in Figure 3.4. Specific capacity is normalized to zero at the beginning of each C/2 charge to aid in visualizing the data. To minimize time at high voltage, where electrolyte oxidation becomes increasingly likely, charging was performed with a constant current-constant voltage (CC-CV) protocol for all three cells. As can be seen, the cells are prevented from exceeding 3.6 V, switching from CC to CV once the voltage maximum is reached. During the CV step, the charge C-rate decays to a cut-off of C/20, at which point the cell is subsequently discharged. For comparison with Cell A, the profiles for eight cycles (also 100 cycles apart) from each full-DOD, C/10 discharge for Cell B (Figure 3.4b) are displayed. The profiles for six full-DOD, C/2 cycles (spaced only 5 cycles apart) for Cell C are also shown (Figure 3.5). As in Figure 3.4, the specific capacity traces in Figure 3.5 are normalized to zero at the beginning of each charge cycle. In Figure 3.4b, however, the specific capacity at the beginning of each full-DOD discharge is normalized to zero (and counted in reverse direction) so that this cell's accessible capacity can be compared over multiple cycles. For Cells A and B, little voltage or capacity differences can be seen after thousands of hours of continuous cycling, indicating nearly reversible electrochemical oxidation and reduction. In contrast to this reversibility, beginning after only 15 cycles, Cell C shows evidence of internal shorting causing massive "over-charging," well beyond the theoretical maximum of 170 mAh/g (Figure 3.5a). We suspect that such over-charge behavior results from lithium dendrite penetration across the soft HPE, which allows for continuous, high-resistance electron leakage to the cathode, referred to as "soft shorting." Soft shorts such as this can result in very low cycling efficiency without causing catastrophic cell failure (complete voltage loss), which explains why 85% of the initial discharge capacity still remains for this cell despite its obvious deterioration.

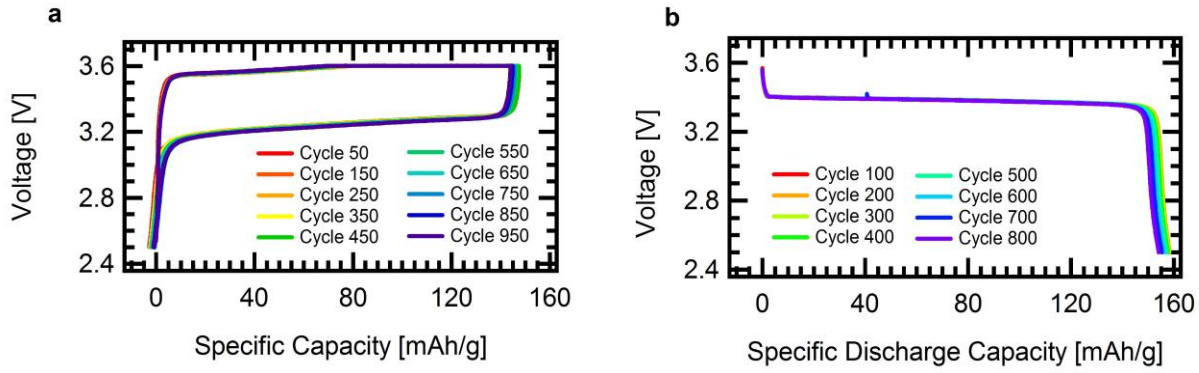

Figure 3.4. Voltage versus specific capacity for two BCPE cells. a. 10 full-DOD cycles (spaced 100 cycles apart) for Cell A (BCPE electrolyte) are normalized to zero at the beginning of charge and indicate nearly reversible electrochemical oxidation and reduction. **b.** 10 full-DOD discharge cycles for Cell B (BCPE electrolyte), normalized to zero at beginning of discharge, demonstrate only a 5.7% loss of specific capacity after 800 C/4 cycles to 80%-DOD.

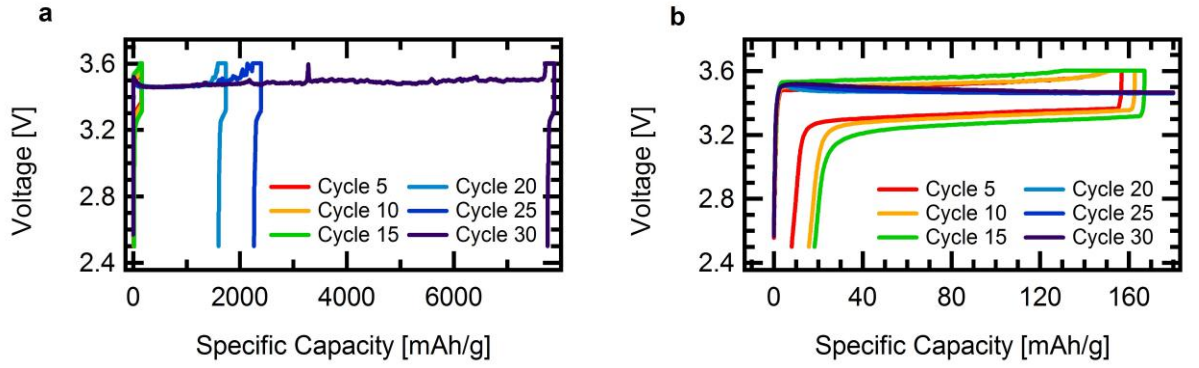

Figure 3.5. Voltage versus specific capacity for an HPE cell. **a.** 6 full-DOD cycles (spaced 5 cycles apart) for Cell C (HPE) depict a "soft-short" occurring between cycle 15 and 20, indicated by over-charging up to > 46 times the theoretical specific capacity (170 mAh/g) by cycle 30. **b.** The smaller-scale plot of Cell C shows increasing resistance on charge and discharge for cycles 5, 10, and 15, followed by a decrease in initial charge resistance for cycles 20, 25, and 30, which supports a diagnosis of lithium dendrite penetration through the separator.

In Figure 3.6, the normalized DC resistance, measured at 50% state of charge (SOC) for each discharge cycle, is shown for Cells A, B, and C. The difference between the measured voltage (V_{Cell}) and the equilibrium voltage (V_{OC}), which between about $0.02 < x < 0.90$ in Li_xFePO_4 is constant at 3.42 V, gives the overpotential (V_{OP}) at a given SOC. From the V_{OP}, the instantaneous DC cell resistance (R_{DC}) can be calculated according to:

$$V_{Cell} = V_{OC} + V_{OP} = V_{OC} + IR_{DC} \tag{3.2}$$

It can be seen that the DC resistance, despite a slight decrease in the first 100 cycles, is nearly constant over 1000 cycles for Cell A. By contrast, Cell B experiences a roughly constant increase in resistance of 0.04% per cycle. This resistance growth helps to explain the marginally higher capacity-fade for Cell B (0.001% per cycle higher) and is probably due to differences in electrode fabrication between the two cells. The resistance of Cell C, however, shows a > 200% increase in resistance occurring rapidly after Cycle 15.

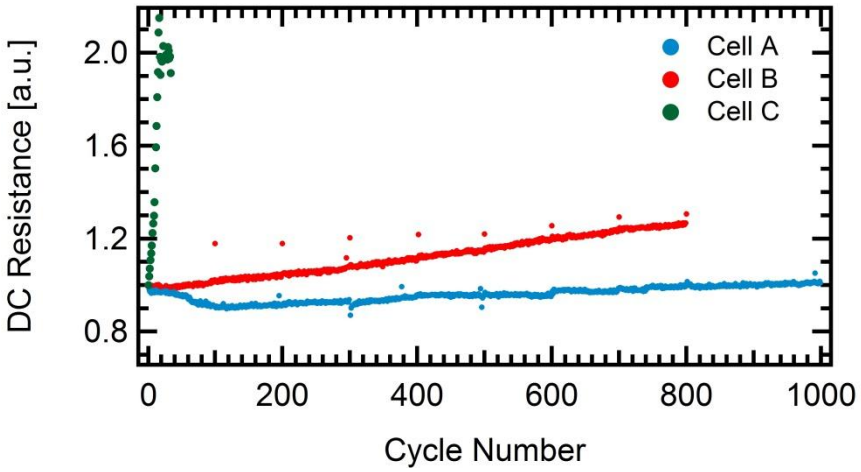

Figure 3.6. Normalized DC resistance for HPE and BCPE Cells. Direct current resistance is normalized in order to compare Cell A (BCPE electrolyte, cycled full-DOD at C/2), Cell B (BCPE electrolyte, cycled at C/4 to 80%-DOD), and Cell C (HPE electrolyte, cycled full-DOD at C/2) versus cycle number. Both BCPE cells show lower resistance gain per cycle compared to the HPE system, though resistance growth is higher for Cell B than Cell A, which we attribute to cell-to-cell electrode variations.

In Figure 3.7a, the coulombic efficiency (Eff_C), expressed as $|C_d/C_c|$, where C is total capacity for a single charge or discharge, gives a measure of the parasitic current contributing to electrolyte breakdown or to electron leakage through the insulating separator. For the duration of the experiment, Eff_C for Cells A and B is very nearly 100%, within the precision of the battery-cycling equipment. This confirms the electrochemical stability of the BCPE, corroborating its low rate of resistance growth. It also indicates that no internal electrical-current leakage is detectable, ruling-out soft internal-shorts due to either dendrite formation or poor mechanical integrity of the separator. By comparison, Cell C shows a high coulombic efficiency initially, but after cycle 15 the efficiency undergoes a rapid decrease that we attribute to an internal short.

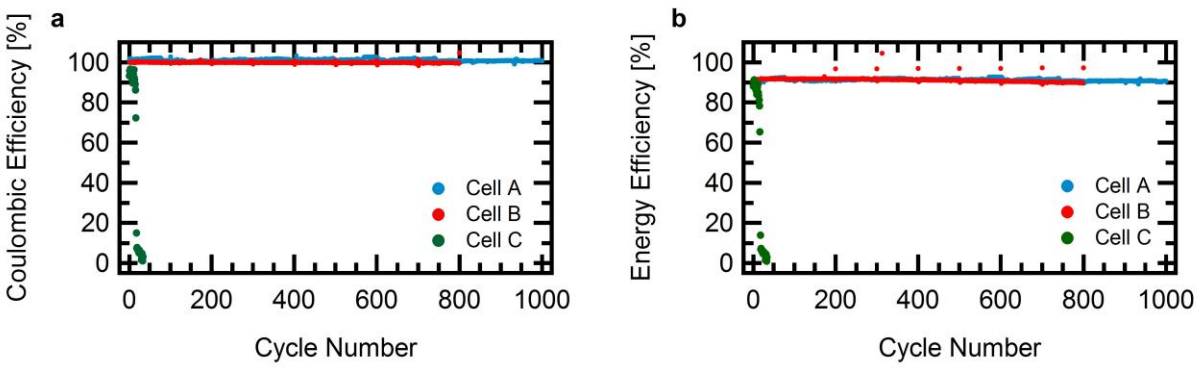

Figure 3.7. Coulombic and energy efficiency for HPE and BCPE cells. a. Eff_C measurements show signs of separator failure (indicative of dendrite formation) on cycle 16 in the soft-HPE system, whereas constant Eff_C in the hard-BCPE system shows no sign of electrolyte degradation by reaction or dendrite formation over hundreds of cycles. **b.** Steady energy efficiency of ca. 90% for Cells A and B demonstrate an additional advantage of the BCPE as compared to the HPE.

In Figure 3.7b, the energy efficiency (Eff_E), which depends on the magnitude of cell resistance as well as the coulombic efficiency, is plotted as a function of cycle number. Eff_E, which factors into operational cost for a battery system, is given by:

$$Eff_E = |E_{\text{discharge}}|/E_{\text{charge}} \tag{3.3}$$

where E is the total energy (Wh) for a single charge or discharge and is related to R_{DC} according to the integral

$$|E| = |\int V_{\text{OC}} I \cdot dt + \int I^2 R_{\text{DC}} \cdot dt| \tag{3.4}$$

Because the discharge current (I_d) and the charge current (I_c) have opposite signs, resistance impacts energy efficiency both by lowering energy output on discharge and by increasing energy input on charge:

$$Eff_E = |E_d|/E_c = \\ |\int V_{\text{OC}} I_d \cdot dt_d + \int I_d^2 (R_0 + R) \cdot dt_d \,]| \,/\, (\int V_{\text{OC}} I_c \cdot dt_c + \int I_c^2 (R_0 + R) \cdot dt_c]) \tag{3.5}$$

R represents additional cell resistance, which increases (or, in rare cases, decreases) with time and cycling. The energy efficiency of any cycle, therefore, is determined by the total cell resistance

$$R_{tot} = R_0 + R \tag{3.6}$$

as well as the total capacity during charge and discharge. In Cells A and B, the total energy efficiency is approximately 90% with a decrease of < 0.3% per 100 cycles, indicating that

cycling introduces minimal efficiency loss to the system. However, primarily due to the rapid decrease in Eff_C, as described above, the energy efficiency of Cell C drops markedly after cycle 15, reaching a low of < 1% for cycle 33.

To corroborate the stable, high coulombic efficiency measured in Cells A and B, containing the block-copolymer electrolyte, a cell very similar to these was cycled, sectioned, and imaged by scanning electron microscopy (SEM) to investigate the lithium electrode surface after repeated lithium plating and stripping. Although electrochemical efficiency measurements can suggest that dendrites have reached across the cell to the positive electrode causing "soft shorts" and reduced efficiency (as in Cell C), SEM allows for the direct visualization of the lithium metal surface, thereby providing additional insight, including whether mossy lithium formations have begun to form in a cell that retains high coulombic efficiency (Cells A and B). In Figure 3.8, a cell cycled 400 times at a C/2 rate was sectioned and imaged and compared to a fresh cell that was never polarized (Figure 3.9). Despite some lithium cracking in both cases, which probably forms during post-mortem sectioning, no evidence of high-surface-area deposits can be seen anywhere in the cycled cell. Furthermore, as opposed to the fresh cell, the cycled cell exhibits perfect contact between the electrolyte and lithium surface after 400 cycles, which indicates that adhesion actually improves during plating and stripping. The adhesive property of the BCPE may explain in part the low resistance gain for cells made from this solid electrolyte.

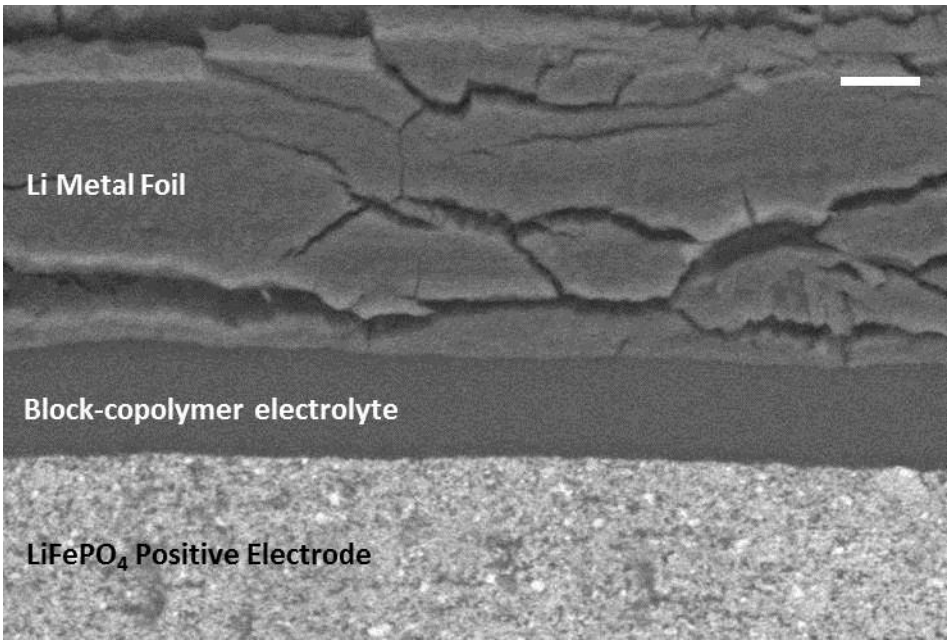

Figure 3.8. SEM of a cycled BCPE cell. After 400 deep-discharge cycles at C/2 rate, a BCPE cell shows no high-surface-area lithium deposits and excellent adhesion between the solid electrolyte and Li metal surface as compared to the pre-cycled cell. Scale bar represents 10 μm.

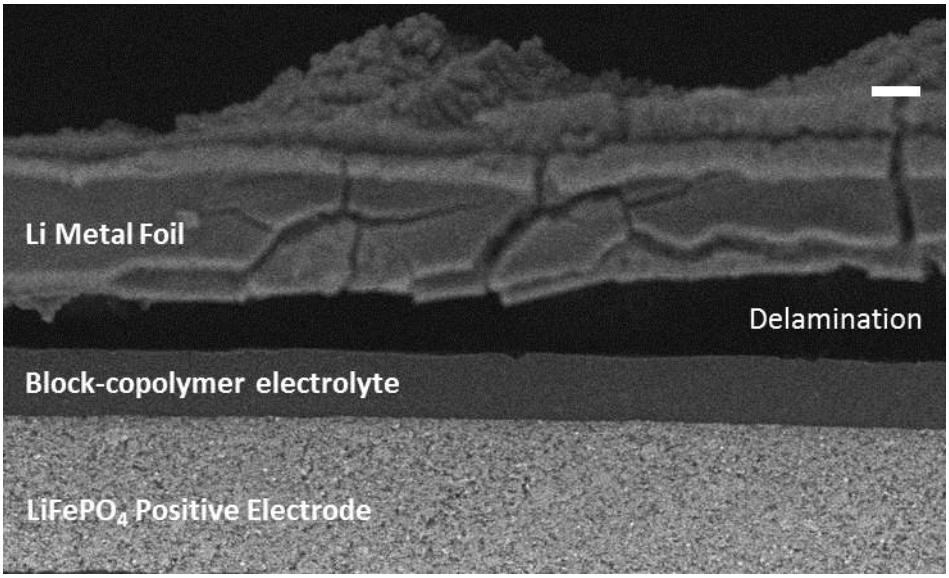

Figure 3.9. SEM of a fresh BCPE cell. A fully assembled, but never cycled, BCPE cell was sectioned for SEM. Poor adhesion between Li and the solid electrolyte is evident. Cracking in the Li foil is expected due to the sectioning procedure and low fracture toughness of the thin metal foil. (Scale bar: 10 μm.)

3.4. Conclusion

Cells containing a hard BCPE, composed of PS-b-PEO and LiTFSI, show nearly reversible electrochemical cycling behavior at elevated temperature for many months of deep-discharge cycling. By comparison, cells containing a soft-HPE composed of PEO-homopolymer and LiTFSI begin to fail after fewer than 20 cycles. The most drastic failure of the softer HPE cells is coulombic efficiency decline, which can be attributed to lithium dendrite formation, as is commonly seen in other soft-polymer and liquid-electrolyte systems. Importantly, we have shown that a hard, nanostructured electrolyte achieves practical rates while also preventing such dendrite growth, as demonstrated by stable DC resistance, high coulombic and energy efficiency, as well as post-mortem imaging by SEM. The dendrite resistance conferred by the BPCE enables nearly reversible rechargeable lithium-metal cycling, which opens the door to a new generation of cells with high specific energy and long life.

3.5. References

1 Ozawa, K. Lithium-ion rechargeable batteries with $LiCoO_2$ and carbon electrodes - The $LiCoO_2$ C system. *Solid State Ionics* **69**, 212-221 (1994).

2 Tarascon, J. M. and Armand, M. Issues and challenges facing rechargeable lithium batteries. *Nature* **414**, 359-367 (2001).

3 Cairns, E. J. and Albertus, P. in *Annual Review of Chemical and Biomolecular Engineering, Vol 1* 299-320 (Annual Reviews, 2010).

4 Takei, K. *et al.* Cycle life estimation of lithium secondary battery by extrapolation method and accelerated aging test. *Journal of Power Sources* **97-8**, 697-701 (2001).

5 Takei, K. *et al.* Performance of large-scale secondary lithium batteries for electric vehicles and home-use load-leveling systems. *Journal of Power Sources* **119**, 887-892 (2003).

6 Choi, S. S. and Lim, H. S. Factors that affect cycle-life and possible degradation mechanisms of a Li-ion cell based on LiCoO2. *Journal of Power Sources* **111**, 130-136 (2002).

7 Ramadass, P., Haran, B., White, R. and Popov, B. N. Capacity fade of Sony 18650 cells cycled at elevated temperatures Part I. Cycling performance. *Journal of Power Sources* **112**, 606-613 (2002).

8 Ramadass, P., Haran, B., White, R. and Popov, B. N. Capacity fade of Sony 18650 cells cycled at elevated temperatures Part II. Capacity fade analysis. *Journal of Power Sources* **112**, 614-620 (2002).

9 Arora, P., White, R. E. and Doyle, M. Capacity fade mechanisms and side reactions in lithium-ion batteries. *Journal of the Electrochemical Society* **145**, 3647-3667 (1998).

10 Zhang, D. *et al.* Studies on capacity fade of lithium-ion batteries. *Journal of Power Sources* **91**, 122-129 (2000).

11 Vetter, J. *et al.* Ageing mechanisms in lithium-ion batteries. *Journal of Power Sources* **147**, 269-281 (2005).

12 Sloop, S. E., Kerr, J. B. and Kinoshita, K. The role of Li-ion battery electrolyte reactivity in performance decline and self-discharge. *Journal of Power Sources* **119**, 330-337 (2003).

13 Brissot, C., Rosso, M., Chazalviel, J. N. and Lascaud, S. Dendritic growth mechanisms in lithium/polymer cells. *Journal of Power Sources* **81**, 925-929 (1999).

14 Orsini, F. *et al.* In situ Scanning Electron Microscopy (SEM) observation of interfaces within plastic lithium batteries. *Journal of Power Sources* **76**, 19-29 (1998).

15 Bhattacharyya, R. *et al.* In situ NMR observation of the formation of metallic lithium microstructures in lithium batteries. *Nature Materials* **9**, 504-510 (2010).

16 Aurbach, D., Zinigrad, E., Teller, H. and Dan, P. Factors which limit the cycle life of rechargeable lithium (metal) batteries. *Journal of the Electrochemical Society* **147**, 1274-1279 (2000).

17 Monroe, C. and Newman, J. Dendrite growth in lithium/polymer systems - A propagation model for liquid electrolytes under galvanostatic conditions. *Journal of the Electrochemical Society* **150** (2003).

18 Monroe, C. and Newman, J. The effect of interfacial deformation on electrodeposition kinetics. *Journal of the Electrochemical Society* **151**, A880-A886 (2004).
19 Monroe, C. and Newman, J. The impact of elastic deformation on deposition kinetics at lithium/polymer interfaces. *Journal of the Electrochemical Society* **152**, A396-A404 (2005).
20 Kanamura, K., Tamura, H., Shiraishi, S. and Takehara, Z. Morphology and chemical-compositions of surface-films of lithium deposited on a Ni substrate in nonaqueous electrolytes. *Journal of Electroanalytical Chemistry* **394**, 49-62 (1995).
21 Singh, M. *et al.* Effect of molecular weight on the mechanical and electrical properties of block copolymer electrolytes. *Macromolecules* **40**, 4578-4585 (2007).
22 Appetecchi, G. B. *et al.* Hot-pressed, solvent-free, nanocomposite, PEO-based electrolyte membranes II. All solid-state Li/LiFePO4 polymer batteries. *Journal of Power Sources* **124**, 246-253 (2003).
23 Wright, R. B. *et al.* Power fade and capacity fade resulting from cycle-life testing of Advanced Technology Development Program lithium-ion batteries. *Journal of Power Sources* **119**, 865-869 (2003).
24 Shim, J., Kostecki, R., Richardson, T., Song, X. and Striebel, K. A. Electrochemical analysis for cycle performance and capacity fading of a lithium-ion battery cycled at elevated temperature. *Journal of Power Sources* **112**, 222-230 (2002).
25 Amine, K., Liu, J. and Belharouak, I. High-temperature storage and cycling of C-LiFePO4/graphite Li-ion cells. *Electrochemistry Communications* **7**, 669-673 (2005).
26 Andersson, A. M., Edstrom, K., Rao, N. and Wendsjo, A. Temperature dependence of the passivation layer on graphite. *Journal of Power Sources* **81**, 286-290 (1999).
27 Asakura, K., Shimomura, M. and Shodai, T. Study of life evaluation methods for Li-ion batteries for backup applications. *Journal of Power Sources* **119**, 902-905 (2003).

Chapter 4

In situ concentration mapping of block copolymer electrolytes by scanning transmission X-ray microscopy

4.1. Introduction

Solid electrolytes have long been investigated as replacements to the conventional organic-based liquids used in contemporary Li-ion batteries.[1-7] Liquid electrolyte instability, including the tendency for dangerous exothermic reactions and incompatibility with high energy lithium metal electrodes,[8-11] has prompted significant effort toward the development of stable solid conductors. In particular, a nanostructured block copolymer electrolyte, poly(styrene-block-ethylene oxide), (PS-b-PEO), has shown recent promise as a lithium-compatible electrolyte material for use in practical high-energy rechargeable systems.[7,12,13] That being said, molecular-scale examination of ion transport in PS-b-PEO, which suffers from mass transport limitations particularly at low temperature, is demanded if rational design is to be employed toward improved materials discovery and next-generation battery development. Due to the size of relevant structural features in the model block copolymer-based material, however, not to mention other components of practical electrochemical cells, a spectroscopic technique with sub-micron resolution is necessary if fundamental chemical transport in these and similar systems is to be explored. Furthermore, validation of mathematical models and experimental measurements such as those reported in the preceding chapters of this work require more detailed chemical and electrical information than can be made readily with standard electrochemical techniques.

Techniques amenable to *in situ* chemical and electrical probing of operating batteries with nanometer resolution are limited. Recent efforts at *in situ* analysis of lithium-based batteries have included neutron radiography,[14] for example, which has provided interesting chemical detail but lacks sub-micron resolution. In order to provide smaller-scale information, perhaps the two most suitable techniques are electron microscopy and X-ray spectroscopy. The former has been used to analyze electrochemical systems *ex situ,* providing chemical information via EFTEM[12] or EDS[15] with near-atomic-level resolution, but *in situ* battery cycling is particularly challenging.[16] Via scanning electron microscopy or transmission electron microscopy, both surface and bulk features can be examined, but high-energy electrons typically cause beam-damage to the organic components of practical cells if experiments are to be performed for any length of time. Furthermore, the high vacuum necessary to maintain electron flux makes the study of liquid materials additionally challenging.

Soft X-rays, with energies less than 1000 eV and wavelengths on the order of 1 nm, provide adequate resolution as well as the ability to collect detailed, and in some cases bulk, chemical and electronic information. Like electron microscopy, soft X-ray methods,

including X-ray emission spectroscopy, often require ultra-high vacuum to prevent interference by atmospheric molecules. However, other X-ray techniques, including X-ray photoelectron spectroscopy (XPS) and X-ray absorption spectroscopy (XAS), have been shown to operate at substantially higher pressures,[17-20] which could make both solid and liquid electrolyte investigation achievable. XPS and XAS are both capable of providing detailed chemical information with different strengths and weaknesses. XPS, for example, is highly surface sensitive, probing only the first few nanometers of an experimental material. XAS, on the other hand, has been recently put to work as a microscopy tool, providing chemical contrast with nanometer-scale resolution on thin materials in a bulk, transmission geometry.[18-20] In this exciting application of near edge X-ray absorption fine structure (NEXAFS), scanning transmission X-ray microscopy (STXM) generates spatially resolved chemical contrast, complementary in many ways to the capabilities of electron-based microscopic techniques. In fact, STMX is particularly well suited to the study of polymeric materials, with X-ray absorption edges in the 200 to 1000 eV range, and has been utilized at beamlines 11.0.2 and 5.3.2 at the Advanced Light Source, Lawrence Berkeley National Laboratory.[20]

In this work, we apply a synchrotron STXM technique to block-copolymer investigation, in which tunable, monochromatic soft X-rays are impinged upon a sample as indicated in Figure 4.1a. Therein, transmission of incident photons through a polymer film (typically 1 micron or thinner) is detected by a photomultiplier tube (PMT) to quantify absorbance by core levels of specific chemical bonding structures of interest. A high degree of electronic structural detail is obtainable by this NEXAFS technique, although herein we use it to quantify elemental composition in polymers that serve as the electrolyte in lithium-based batteries. The materials investigated are nanostructured solid electrolytes composed of PS-b-PEO containing a dissolved lithium bis(trifluoromethane)sulfonimide salt (LiTFSI). In particular, we seek to measure changes in LiTFSI concentration throughout electrolytes within operating batteries at the sub-micron scale. Synchrotron STXM is very well suited to this application because high photon flux and a precise piezo-controlled sample stage permit very short exposure times (on the order of ms) and high spatial resolution; as a result, the collection of rapid temporal information on *in situ* systems is possible.

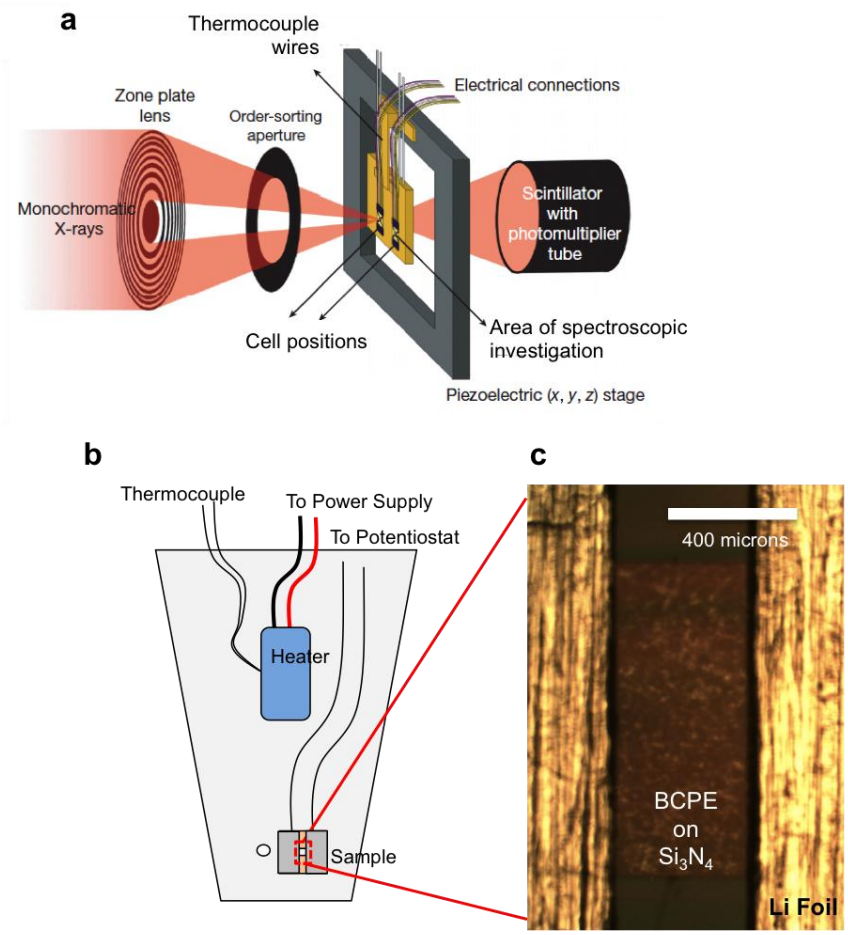

Figure 4.1. Experimental STXM setup. a. The scanning transmission X-ray microscopy (STXM) setup shows the arrangement of incident X-rays, sample, and photon detector. **b.** A home-built sample holder is affixed with a restive heater, thermocouple, and electrical leads connecting to the solid-state lithium battery. **c.** An optical microscope image shows the electrochemical cell geometry, including the block copolymer electrolyte (BCPE) region under investigation and the two lithium foil electrodes. The total active surface area of each lithium foil is 5 mm x 4.8 mm.

With this technique, we perform high-resolution lithium salt concentration mapping on *in situ* all-solid-state metallic-lithium batteries. In so doing, we provide the first sub-micron-scale measurements on ion gradient evolution, with temporal detail on the order of minutes, within battery electrolytes; we also describe a general approach toward performing fundamental *in situ* characterization on these and similar electrochemical systems. Furthermore, we apply this technique toward the direct, fundamental measurement of lithium transference in a polymer electrolyte battery, pointing out the advantages of STXM as compared to traditional electrochemical approaches.[21-24] Via local salt concentration data, we also identify in real time the appearance and disappearance, during galvanostatic charge and discharge, of salt precipitates in nanostructured PS-b-PEO

containing LiTFSI, which warrants future study by this and related spectroscopic approaches.

4.2. Experimental

Poly(styrene-block-ethylene oxide) (55/45 wt/wt%) was synthesized by anionic polymerization as described previously.[7] LiTFSI was purchased from Ferro and used without purification. To make electrolyte films, LiTFSI was dissolved at the appropriate concentration along with block copolymer in cyclohexanone (10 wt% polymer) and spin-cast (2800 rpm for 30 s) onto 5 mm by 5 mm silicon wafers (high resistivity) covered uniformly with 50 nm thick silicon nitride films (Silson Ltd.). Spin-cast electrolyte films cover the entire 25 mm^2 substrate. A square hole (1.0 mm x 1.0 mm) in the center of the silicon substrate, but not the silicon nitride or electrolyte layers, provides an X-ray pathway for spectroscopic investigation. Prior to cell fabrication, electrolytes were dried thoroughly by heating to 90 °C on a hot plate. Electrolyte films for use as salt concentration standards and in electrochemical cells are made by the same procedure. The dry electrolyte thickness for all samples is approximately 1100 nm ± 12 nm as determined by AFM.

To fabricate lithium symmetric cells for *in situ* electrochemical and spectroscopic analysis, lithium foil electrodes (Chemetall Corporation, 30 micrometer thickness) were cut with a razor blade and laminated gently to dry, solid electrolyte films at 90 °C (Figure 4.1c). Lithium electrode dimensions were approximately 5 mm x 4.8 mm, and electrodes were placed by hand symmetrically on either side of the silicon wafer substrates, separated by approximately 0.4 mm, which serves as the exposed electrolyte region for spectroscopic analysis. Optical microscope images were taken of cells prior to X-ray investigation. All cell fabrication steps were performed in an argon-filled glovebox (< 1 ppm H_2O) or in a dry room (<0.5% RH). Cells were transported to the synchrotron beamline in hermetically-sealed polymer-coated aluminum bags and inserted to the STXM sample chamber under flow of inert gas.

Home-built cell holders for STXM were made of aluminum (Figure 4.1b) affixed with a DC resistance heating pad. Temperature was controlled at 80 °C with a 24 V variable DC controller and monitored by a thermocouple. The measured temperature differential between the thermocouple and the cell was < 1 °C. Electrical connections between lithium and the electrical leads were made via pressing the top surface of each lithium electrode onto copper mesh current collectors, which were taped in place on the cell holder and welded to wires routed to a vacuum feed-through. External direct current measurements via these feed-through wires were made with a Keithley 2440 sourcemeter controlled by a PC. Absolute currents were in the range of 10 to 100 nA.

X-ray spectroscopy measurements were performed at Beamline 5.3.2.2 at the Advanced Light Source, Lawrence Berkeley National Laboratory. The sample chamber was filled with

1/3 atm He for thermal conduction, and X-ray energies were varied, with better than 1 eV resolution. Raw data were processed as described below using Igor Pro software.

4.3. Results and Discussion

In order to quantify salt concentrations in solid-electrolyte samples, a number of standards with varying salt concentration were made for near-edge X-ray-absorption-fine-structure (NEXAFS) spectroscopy using the synchrotron STXM instrument. Electrolyte films of comparable thickness to those for use in electrochemical cells, with *r* values between 0 and 0.22, were analyzed, where *r* value represents the molar ratio of lithium ions [Li^+] in the dissolved LiTFSI salt to ethylene oxide units [EO] in the block copolymer chain, and can be converted to salt molarity with a known electrolyte density. Because the Li 1s orbital is too low energy to be investigated by this instrument, F 1s core levels were probed by tuning the synchrotron photon energy to between 670 and 730 eV. Assuming electroneutrality throughout the electrolyte at the length scale of interest, F concentration serves as a proxy for Li concentration throughout this work.

As seen in Figure 4.2a, the resulting F 1s absorbance peaks are related to the transmitted X-ray intensity through the electrolyte films and measured at the photomultiplier tube (PMT) (Figure 4.1a) according to

$$A = -\log\left(\frac{I}{I_0}\right) \tag{4.1}$$

where A is the absorbance and I/I_0 is the transmittance, or photon intensity passing through the sample, I, relative to that of a reference, I_0, in this case a PS-b-PEO film containing no LiTFSI. By using the photon intensity transmitted through salt-free PS-b-PEO as I_0, the total absorbance at the F 1s absorption peak is corrected for the cross-section of non-fluorine substituents in the polymer films.

To minimize X-ray exposure and improve time resolution, a simple ratio of the corrected absorbance at the F 1s absorption peak (692 nm) was compared to that just before the absorption edge (685 nm) such that only two energies (rather than an energy scan) need to be measured to determine the fluorine concentration at any location. The following expression describes the corrected absorption ratio describing the relative quantity of fluorine in an electrolyte film of constant thickness:

$$\text{Abs ratio} = -\ln\left[\left(\frac{I_{692}}{I_{685}}\right)\left(\frac{I_{0,685}}{I_{0,692}}\right)\right] \tag{4.2}$$

where I is the intensity of X-rays at the specified wavelength reaching the detector.

Equation 4.2, therefore, is used to convert raw photon transmission data to salt concentration for the purpose of concentration mapping in electrochemical cells. In Figure

4.2b, the calibration curve describing the linear dependence of salt concentration on the corrected F 1s absorbance ratio is shown. By this linear relation, the precise determination of lithium salt *r* value anywhere in the detection region of the electrolyte (Figure 4.1c) can be found. For electrochemical measurements described later in the text, the salt molar ratio can also be converted to salt molarity. According to a reported density dependence of PEO on dissolved LiTFSI quantity (Figure 4.2c), the relationship between *r* value and molar concentration for LiTFSI in this system is depicted in Figure 4.2d. A constant PS density of 1.06 g/mL is used to find the total block copolymer density, which varies between 1.10 and 1.35 g/mL depending on amount of salt.

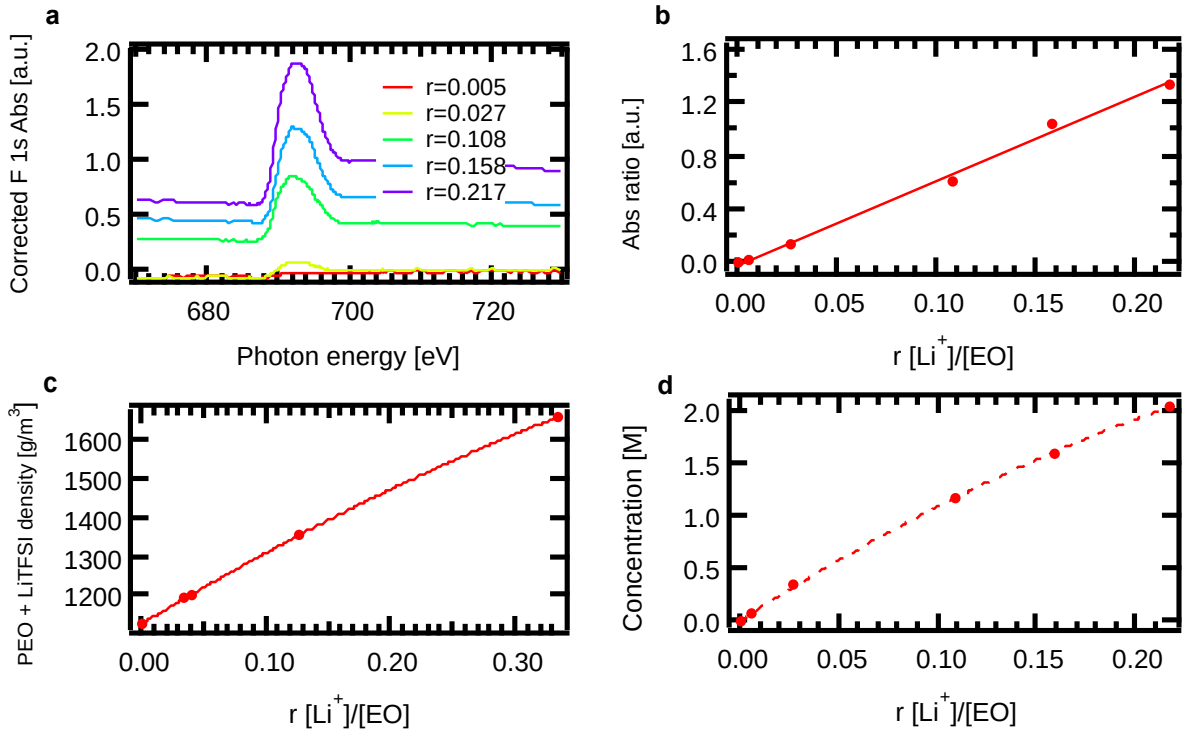

Figure 4.2. Salt concentration standards: absorption and correlations to concentration. a. F 1s absorbance between 670 eV and 730 eV, normalized to the PS-b-PEO standard with no salt, shows distinct, concentration-dependent absorption peaks. The ratio of abs at the peak energy (692 eV) to that just before the absorption edge (685 eV) is used to quantify fluorine concentration. **b.** The F 1s absorbance ratio, corrected according to $-\ln([I_{(692)}/I_{(685)}]*[I_{0,(685)}]/I_{0,(692)}])$, shows a linear dependence on salt *r* value $[Li^+]/[EO]$. **c.** The reported density of homopolymer-PEO containing LiTFSI versus salt concentration is given and used to convert between *r* value and molar LiTFSI concentration in PS-b-PEO. **d.** The density-dependent relationship between molarity and *r* value in the PS-b-PEO: LiTFSI system is shown with a fit depicted by the dashed line.

Concentration mapping on *in situ* electrochemical cells was performed with absorption data, generated as described above, acquired across an electrolyte region between lithium

electrodes, either at rest or during polarization. The cells under investigation are pictured in Figure 4.1c and are composed of two symmetric lithium electrodes, separated by the block copolymer electrolyte, approximately 400 micrometers in thickness. As per Figure 4.1b, the samples are attached to a homebuilt cell holder, which can be precisely heated by a resistive heater to 80 °C to enhance ion conduction. The areas exposed for X-ray absorption spectroscopy were rectangular sections 10 μm tall (parallel to electrode surfaces) by 420 μm wide, spanning the entire distance between electrodes and including the electrode edges. Scanning was performed by rastering the sample holder such that a time-average (approximately 5 min) across the sample was achieved during exposure, with no measurable time-bias toward either electrode. The 10 x 420 μm maps were converted to one-dimensional line scans by averaging in the 10-μm vertical direction. For purposes of the experiment, it was assumed that no significant variation exists in this direction (i.e., parallel to the electrode-electrolyte interface in each cell), such that a concentration profile across the electrolyte can be taken anywhere top to bottom with the same results. This assumption depends on uniform current density and will be discussed later in the text. Individual pixels in the mapped regions were derived from 100 nm exposure regions (defocussed photon beam diameter) taken at 16,800 unique positions (40 vertical positions by 420 horizontal positions, each spaced evenly apart). That is to say, horizontal resolution was 1 μm, while vertical information (0.25 nm resolution) was summed to improve signal to noise. To reduce issues related to beam damage, the exposure region was moved top to bottom in 10 μm increments after each measurement, which also assumes no concentration dependence on vertical position.

The resulting concentration profiles for 3 lithium symmetric cells of different bulk salt concentration are seen in Figure 4.3. Each cell was heated to 80 °C and then charged at a constant current, beginning from an equilibrium condition. Salt concentration, as it evolves in the cell during polarization, is displayed versus one-dimensional position across the electrolyte for each cell. In all cases, color advances in rainbow order with time, and no vertical position information is included. Before cell polarization (red traces), the salt concentration is uniform across the cells, indicating equilibrium. By the second scan, however, after just a few minutes, changes in concentration become evident in all three systems. As can be seen, salt gradients develop quickly under applied current: line scans represent an average over a ca. 5 min acquisition window, spaced ca. 5 min apart. During polarization, salt depletion takes place at the cathode (right side) where Li^+ ions are reduced and plating occurs, while salt accumulation takes place at the anode (left side) where Li^+ ions are created, building up near the electrode surface. Net lithium ion flux is from left to right. Initially, changes are evident only adjacent to the electrodes, but propagation of the gradient fronts evolves as the salt responds to developing diffusion forces. In the 0.3 and 0.6 M cells, salt concentration after the first few scans approaches 0 on the right side of the cells. On the other hand, in the 1.2 M cell, the gradient continues to increase, ultimately approaching a steady state prior to 2 h.

It can also be seen that in the 1.2 M cell (Figure 4.3a), a much larger salt gradient is established than in the cells with lower concentration (Figure 4.3b and 4.3c). The

dependence of the maximum gradient on bulk salt concentration, c_b, is straightforward, expressed for a linear gradient by

$$\nabla c_{\max} = \frac{2c_b}{L} \tag{4.3}$$

where L is the distance between electrodes. However, the time- and current-dependent concentration behavior across a real electrolyte is not usually so simple. In real electrolyte systems, liquid or solid, concentration-dependent transport properties cause variation in the concentration gradient within a polarized system.[25-27] Any deviation of the gradient from linearity, caused by differences in the salt diffusion coefficient or lithium transference at different salt molarities, can be quantified by this technique. Spatially-resolved information such as that provided here, therefore, is critically important for corroborating first-principles mathematical simulations.

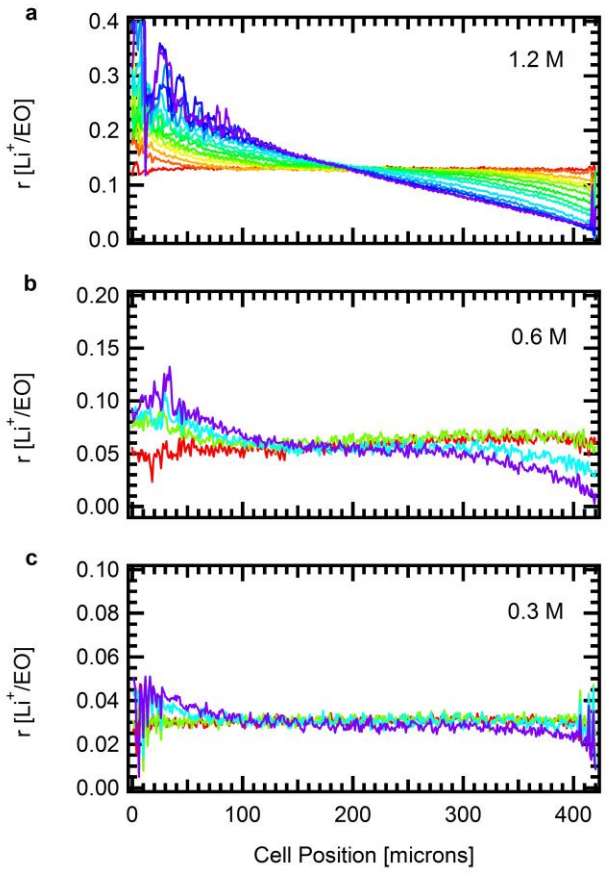

Figure 4.3. Salt concentration versus time and cell position. a. The salt concentration versus time (rainbow order) across a 420 μm wide PS-b-PEO electrolyte, containing 1.2 M LiTFSI, shows the establishment of a steady-state gradient between Li electrodes. **b.** The concentration gradient in a cell with only 0.6 M LiTFSI reaches 0 Li^+ concentration at the cathode (right side) before establishment of a linear gradient. **c.** At even lower salt concentration, salt depletion takes place very quickly in the 0.3 M electrolyte system.

In Figure 4.4, the electrical potential of each cell is also displayed (Figure 4.4b) along with its applied current density versus time (Figure 4.4c) and the maximum salt gradient for that system (Figure 4.4a). As described, the samples with higher salt concentration can sustain a larger gradient (and, thus, larger current density) before reaching a runaway overpotential. The two lower concentration cells are charged at ca. 0.5 mA/cm^2, while, to stress the gradient in the high concentration system, the 1.2 M cell is charged at ca. 1.0 mA/cm^2 (Figure 4.4c). As seen in Figure 4.4b, before 30 min, a rapid increase in potential is evidenced for the 0.3 and 0.6 M systems, while the 1.2 M sample, even at twice the current density, continues for 2 h before being set to rest without reaching the predefined cutoff potential of 1 V. As illustrated, the onset of nonlinear voltage, evidence of the limiting current, can be related directly to an *in situ* concentration measurement: salt depletion at the cathode surface, indicated in Figures 4.3 and 4.4 for the 0.3 and 0.6 M cells, results in rapid, unsustainable voltage spikes. The maximum gradients for all three systems (Figure 4.4a), which are converted from *r* value to molarity according to the fit in Figure 4.2d, provide micron-scale detail relating the salt concentration data directly to measured external cell potential. While the 1.2 M cell also shows salt depletion near the cathode surface, it does so only after nearly 2 h; and although the cell voltage is still increasing at this point (Figure 4.4b), it is turned to rest before the voltage runs away.

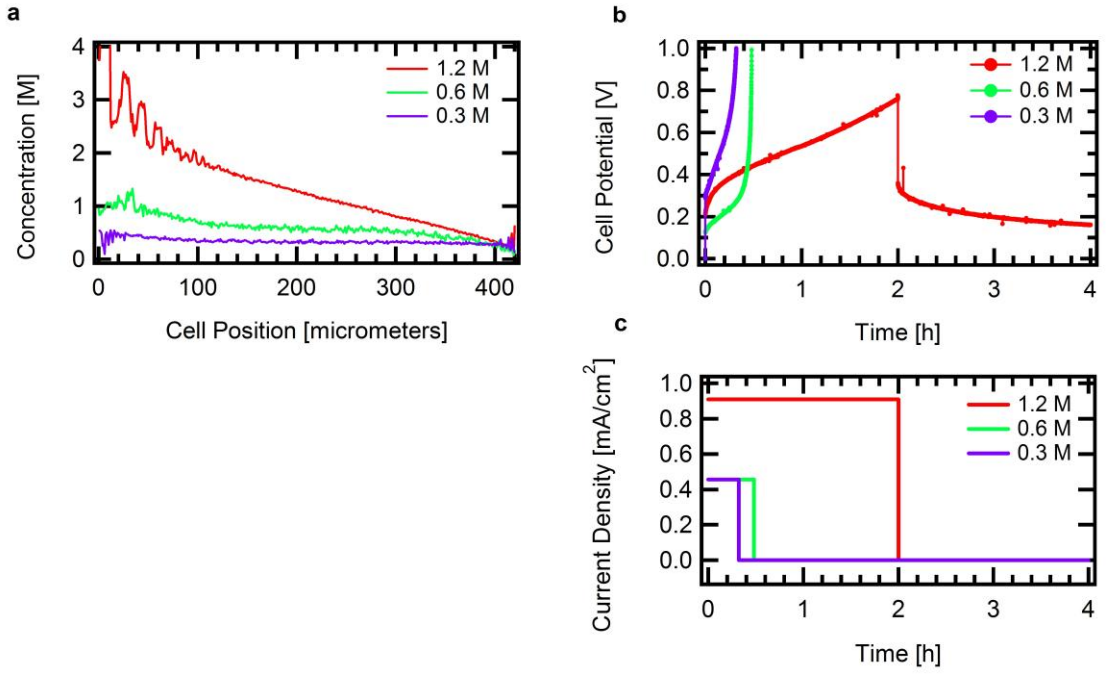

Figure 4.4. Salt gradient and potential measurements for Li symmetric cells containing 3 bulk salt concentrations. a. Maximum measured gradients in 3 cells demonstrate how higher bulk salt concentration allows for larger gradients and, thus, larger current densities. **b.** Potential versus time for the 3 cells shows rapid potential increases for the 0.3 and 0.6 M samples due to depletion of salt at the cathode surface before establishment of a steady-state salt gradient. **c.** The low concentration cells were charged at ca. 0.5 mA/cm^2 until hitting a cut-off of 1 V, while the 1.2 M cell was charged at approximately twice that rate, 0.9 mA/cm^2, for a preset time of 2 h before resting.

The 1.2 M sample is able to sustain a current density of approximately 0.9 mA/cm^2 for 2 h; however, after as little as 1 h, irregularity is observed in its concentration versus position profiles (Figure 4.3a and 4.4a). Near the anode surface, at high concentrations, peaks in the 1D line scans become evident, demonstrating a salt concentration as high as r=0.4 (or greater than 4 M). These peaks are variable in position but occur at regular intervals, with a peak-to-peak distance on the order of 10 μm. To explore the identity of these anomalies, two-dimensional maps of salt concentration, with a spatial resolution of 0.25 x 1 μm, were also utilized.

Figure 4.5 shows the time series of these 2D maps for the cell containing 1.2 M LiTFSI during charging and subsequent rest. In contrast to the line scans presented in Figure 4.3, herein, the salt concentration across the electrolyte is not summed in the vertical direction, allowing for sub-micron vertical resolution in addition to 1-micron horizontal resolution. As can be seen, the alternating peaks are resolved as roughly-circular regions, often as large as 10 μm across, of high salt concentration, which advance progressively from the anode surface into the center of the electrolyte during charging. It is notable that while the *r* values indicated by yellow in these maps exceed 0.4, or nearly 4 times the bulk concentration in this sample, they represent an average through the sample depth; as a result, they could contain regions of even higher fluorine concentration near the electrolyte surface where we expect the highest current density.

Additional investigation must take place to confirm the identity of what appears to be local salt precipitates; but in any case, it is interesting to find such non-uniform concentration in these nanostructured samples. For a more detailed salt concentration map, Figure 4.6 presents a smaller-scale area, depicting the concentration of LiTFSI in the polymer electrolyte at a location near the anode surface at the end of charging. This 20 x 20 μm region illustrates approximately 2-fold variation in salt molarity from the center of the precipitates to the surrounding matrix. With this in mind, it should be pointed out that electrolyte in this sample has approximately the same bulk LiTFSI concentration as the solid electrolytes used in Li/$LiFePO_4$ cells that cycle reversibly for hundreds of cycles, as reported in Chapter 3. We must conclude, therefore, that the non-uniform salt distribution, if it also occurs in those practical cells, is highly curious though non-damaging to cycling performance. Furthermore, during rest in these Li/Li cells, the local concentration variations begin to disappear, with 2 h being nearly enough time for the salt concentration to return to equilibrium (Figure 4.5). It was also found that over subsequent charge and discharge cycles on these samples, formation and dissolution of the precipitates is reversible and occurs similarly on both sides of the electrolyte, depending only on the current direction.

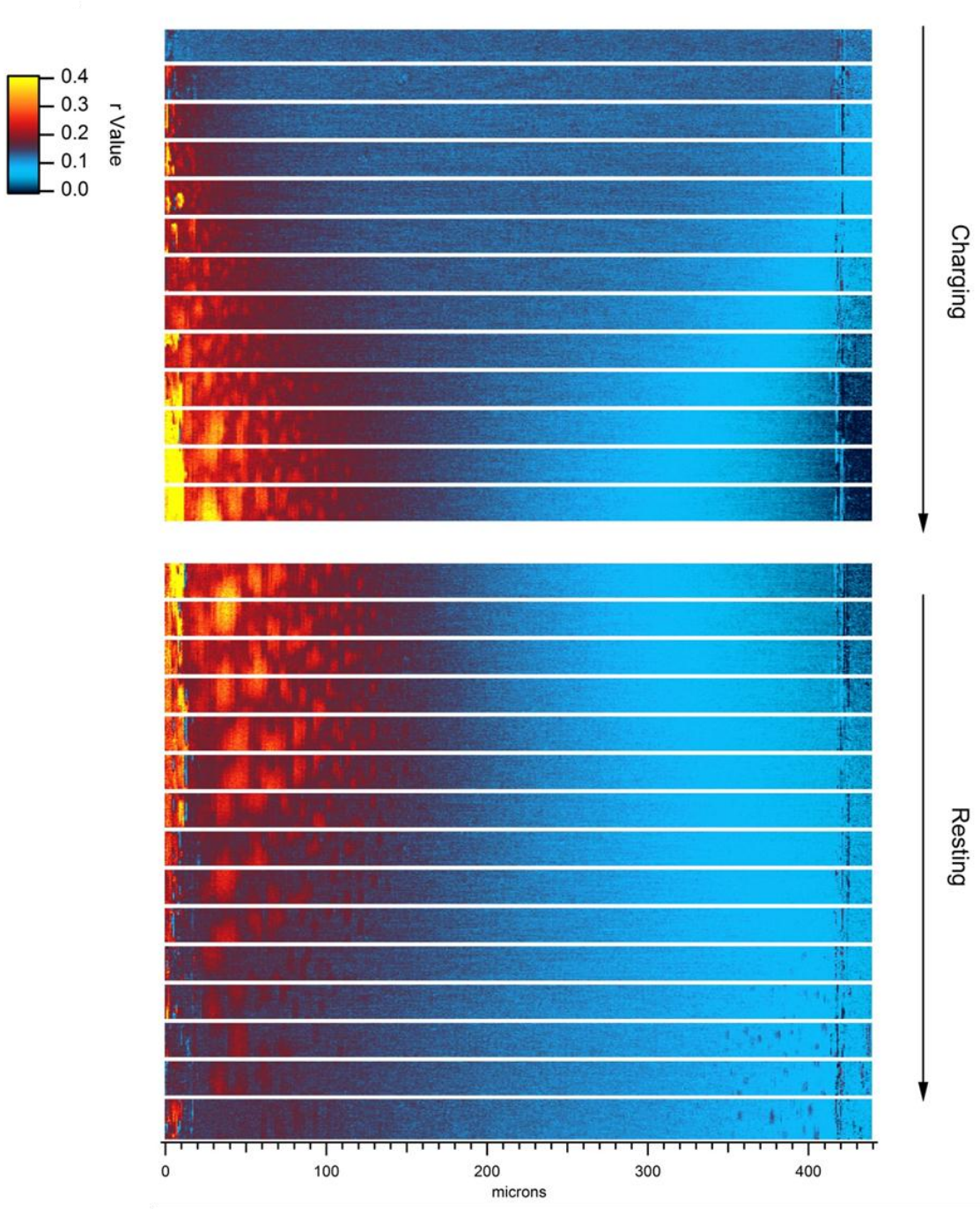

Figure 4.5. Salt concentration maps, evolving with time during charge and rest. 10 x 440 μm maps show the evolution of a salt concentration gradient with time, as well as localized high concentration regions adjacent to the lithium anode (left side). These features develop during charging but (nearly) disappear over two hours of rest. The direction of ion flow during charging is left to right. The *r* value $[Li^+]/[EO]$ color scale goes from 0 to 0.4 (legend: top left)

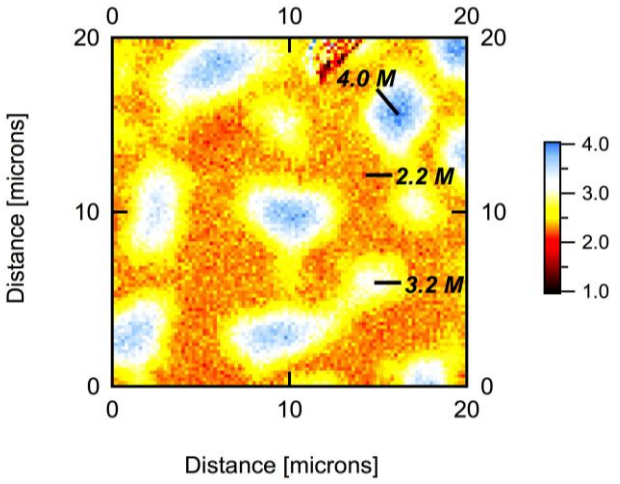

Figure 4.6. Localized regions of high salt concentration formed during charging. Several μm-diameter regions of high fluorine concentration depict likely salt precipitates in a surrounding medium containing much lower LiTFSI content. The 400 μm^2 map was taken of a representative region adjacent to the lithium anode in a 1.2 M cell.

It is clear that STXM provides a powerful tool for making fundamental measurements in this lithium-based system. Using the concentration maps presented herein, therefore, we seek to demonstrate the calculation of lithium transference, a fundamental transport property that remains under much debate in the electrochemical community and is of great interest to the field. Transference is the fraction of charge carried by a particular species in an electrolyte of uniform composition, and its value is important to battery operation because it determines the magnitude of concentration gradients that develop during battery cycling.[26] Lower values of lithium transference cause larger gradients, higher overpotential losses, and reduced power performance. The precise description of the overpotential losses due to a concentration gradient is given according to concentrated solution theory by[25]

$$\nabla\Phi = -\frac{i}{\kappa} + \frac{2RT}{F}\left(1 + \frac{d\ln f_{\pm}}{d\ln c}\right)\left(1 - t_{+}^{0}\right)\nabla \ln c \qquad (4.4)$$

where i is the current density in the electrolyte, κ is the ionic conductivity, $\nabla\Phi$ is the electrochemical potential gradient measured with respect to a reference electrode probe reversible to Li^+, F is Faraday's constant, t_+^0 is the lithium transference, and $f_\pm$ is the salt activity. Equation 4.4 demonstrates that a larger value of t_+^0 results in a smaller $\nabla\Phi$.

Despite its importance to battery performance, however, transference is a difficult property to measure, especially by standard electrochemical techniques, because it does not relate in a straightforward way to electrochemical potential as measured by external leads from a battery. Equation 4.4 illustrates that both the salt activity and the concentration gradient, as well as their precise variations across a cell, must be known to

permit the determination of transference by an external potential measurement. In Chapter 2 we reported a novel method for measuring lithium transference in solid electrolytes such as PS-b-PEO that does not rely on knowledge of the salt activity, but herein, an *in situ* technique may provide a much more straightforward approach.

According to the following equation, the transference is also related to the salt concentration gradient at steady state by

$$(1 - t_+^0) = \frac{-FD\nabla c}{i} \tag{4.5}$$

where D is the salt diffusion coefficient, and i is the current density. This relation comes from the balance of anion fluxes, diffusion and migration, which define the steady-state condition. Previous experimental challenges toward measuring t_+^0 by equation 4.5 come from the difficulty of finding ∇c directly. Herein, a facile determination is possible, direct from *in situ* STXM data, and this can be used to calculate the lithium transference for a range of salt concentrations under steady-state conditions.

In Figure 4.7, a representative steady-state concentration gradient is determined by linear fit located around the center of a cell at the bulk concentration of 1.2 M LiTFSI. The gradient derived from the fit, as seen in the figure annotation, is -0.00512 M/micron. With an estimated average current density of 0.9 mA/cm^2, and a diffusion coefficient for this concentration of 3.2 x 10^{-8} cm^2/s (see Chapter 2), equation 4.5 can be used to calculate t_+^0. In so doing, we report a value of t_+^0 at 80 °C, for this PS-b-PEO system with 1.2 M LiTFSI, of 0.83. However, previous values determined by potentiostatic polarization and the limiting current method are much lower – close to 0.2 – as are reported transference figures for the related homopolymer-PEO:LiTFSI system by a variety of methods.[22,23,28,29] Therefore, we believe our calculation does not represent the true value for this system.

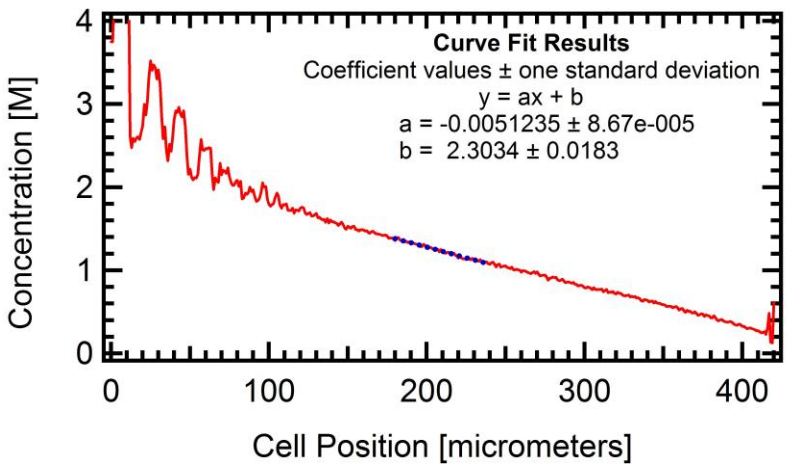

Figure 4.7. Concentration gradient used to calculate the lithium transference. At the center of the 1.2 M cell, a linear fit to the salt molarity versus cell position determines a concentration gradient of -0.00512 M/μm.

Despite the probable inaccuracy of this initial measurement, we assert that a straightforward means of measuring the lithium transference has been proposed. In this case, it is our assumption that insufficient knowledge of the local current distribution prevents a more accurate calculation. For example, equation 4.5, from which t_+^0 is derived, assumes uniform current density across the polymer film. In these samples, we believe that the current density was not uniform throughout. For example, the active region of the cell extends across the entire wafer, which is 5 mm wide, but the width of the analyzed region was limited to 1 mm, defined by the dimensions of the silicon nitride window. Furthermore, measurements reported in Figure 4.3 and 4.4 were taken on a smaller, ca. 100 micrometer, region to limit the distance traveled by the sample stage during the experiment. As a result, the data used to calculate lithium transference were collected on a small region of the entire film. Isolated measurements made further apart across the window uncovered variations in the salt distribution, including a nearly flat concentration profile during polarization in some locations, indicating that the current distribution was indeed non-uniform. While a proper cell must have uniform current density parallel to the electrode surfaces, in this hand-built cell uneven electrode-electrolyte contact (established by gentle pressing) could cause differences in surface resistance and, thus, local current density throughout the sample. In the worst case, complete lack of contact between the lithium foil electrode and the hard block copolymer electrolyte at isolated points would prevent the flow of ionic current in certain regions of the film, explaining the flat concentration profile observed in a few locations. Therefore, we expect current-density variations to be the most likely explanation for our overestimate of transference. By future measurements of the concentration gradient in additional regions of the cell, or by making cells with smaller lithium electrodes, such that the entire active electrolyte area can be investigated, we may test this hypothesis.

Another possibility for error arises from grain structure in these microsphase-separated polymer films. While sample thickness was found to vary by only ca. 10% in these electrolyte castings, block copolymer grain structure, especially in a thin electrolyte, could also play a role in current density inhomogeneity and deceptive transference calculations. Because typical grains are approximately 1 micrometer in related block copolymer systems,[7] with a thickness of only 1 μm, the thin samples studied herein present another possible measurement issue. By similar measurements on a homopolymer-PEO electrolyte, which should not have grain structure, we can also address this possibility. Because the attenuation lengths are quite long for this material (> 1 μm for the F 1s region), measuring thicker samples might also be an achievable solution, reducing the chance for single grains oriented in the wrong direction to block significant current flow. Alternatively, a block copolymer with smaller domain size, different microphase structure, or smaller grain size could also be investigated.

4.4. Conclusion

Using synchrotron scanning transmission X-ray microscopy (STXM) we have generated the first sub-micron *in situ* salt concentration maps on lithium metal batteries by way of quantitative near-edge X-ray absorption fine structure measurements. By this approach we produce significant detail on the kinetics of the solid-state block copolymer electrolyte, PS-b-PEO containing LiTFSI, for direct comparison with theoretical and experimental data. Furthermore, we report a methodology for determining fundamental transport properties including the lithium transference number, which is calculated and reported for this system at 80 °C. It is clear that STXM, as developed herein, is a powerful technique, which can be adapted generally to *in situ* electrochemical analysis on this and related electrochemical systems.

4.5. References

1 Meyer, W. H. Polymer electrolytes for lithium-ion batteries. *Advanced Materials* **10**, 439 (1998).

2 Croce, F., Appetecchi, G. B., Persi, L. and Scrosati, B. Nanocomposite polymer electrolytes for lithium batteries. *Nature* **394**, 456-458 (1998).

3 Baril, D., Michot, C. and Armand, M. Electrochemistry of liquids vs. solids: Polymer electrolytes. *Solid State Ionics* **94**, 35-47 (1997).

4 Abraham, K. M., Jiang, Z. and Carroll, B. Highly conductive PEO-like polymer electrolytes. *Chemistry of Materials* **9**, 1978-1988 (1997).

5 Fan, L. Z., Dang, Z. M., Nan, C. W. and Li, M. Thermal, electrical and mechanical properties of plasticized polymer electrolytes based on PEO/P(VDF-HFP) blends. *Electrochimica Acta* **48**, 205-209 (2002).

6 Berthier, C. *et al.* Microscopic investigation of ionic-conductivity in alkali-metal salts poly(ethylene oxide) adducts. *Solid State Ionics* **11**, 91-95 (1983).

7 Singh, M. *et al.* Effect of molecular weight on the mechanical and electrical properties of block copolymer electrolytes. *Macromolecules* **40**, 4578-4585 (2007).

8 Chen, Y. F. and Evans, J. W. Thermal analysis of lithium-ion batteries. *Journal of the Electrochemical Society* **143**, 2708-2712 (1996).

9 Bandhauer, T. M., Garimella, S. and Fuller, T. F. A Critical Review of Thermal Issues in Lithium-Ion Batteries. *Journal of the Electrochemical Society* **158**, R1-R25 (2011).

10 Aurbach, D., Zinigrad, E., Teller, H. and Dan, P. Factors which limit the cycle life of rechargeable lithium (metal) batteries. *Journal of the Electrochemical Society* **147**, 1274-1279 (2000).

11 Crowther, O. and West, A. C. Effect of electrolyte composition on lithium dendrite growth. *Journal of the Electrochemical Society* **155**, A806-A811 (2008).

12 Gomez, E. D. *et al.* Effect of Ion Distribution on Conductivity of Block Copolymer Electrolytes. *Nano Letters* **9**, 1212-1216 (2009).

13 Panday, A. *et al.* Effect of Molecular Weight and Salt Concentration on Conductivity of Block Copolymer Electrolytes. *Macromolecules* **42**, 4632-4637 (2009).

14 Siegel, J. B. *et al.* Neutron imaging of lithium concentration in LFP pouch cell battery. *Journal of the Electrochemical Society* **158**, A523-A529 (2011).

15 Brazier, A. *et al.* First cross-section observation of an all solid-state lithium-ion "Nanobattery" by transmission electron microscopy. *Chemistry of Materials* **20**, 2352-2359 (2008).

16 Wang, C. M. *et al.* In situ transmission electron microscopy and spectroscopy studies of interfaces in Li ion batteries: Challenges and opportunities. *Journal of Materials Research* **25** (2010).

17 Zhang, C. J. *et al.* Measuring fundamental properties in operating solid oxide electrochemical cells by using in situ X-ray photoelectron spectroscopy. *Nature Materials* **9** (2010).

18 Drake, I. J. *et al.* An in situ cell for characterization of solids by soft x-ray absorption. *Review of Scientific Instruments* **75**, 3242-3247 (2004).

19 Warwick, T. *et al.* A new bend-magnet beamline for scanning transmission X-ray microscopy at the Advanced Light Source. *Journal of Synchrotron Radiation* **9**, 254-257 (2002).
20 Muntean, L. *et al.* Chemical mapping of polymer photoresists by scanning transmission x-ray microscopy. *Journal of Vacuum Science and Technology B* **23**, 1630-1636 (2005).
21 Doyle, M. and Newman, J. Analysis of transference number measurements based on the potentiostatic polarization of solid polymer electrolytes. *Journal of the Electrochemical Society* **142**, 3465-3468 (1995).
22 Dai, H. L. and Zawodzinski, T. A. Determination of lithium ion transference numbers by electrophoretic nuclear magnetic resonance. *Journal of the Electrochemical Society* **143**, L107-L109 (1996).
23 Bruce, P. G., Hardgrave, M. T. and Vincent, C. A. The determination of transference numbers in solid polymer electrolytes using the Hittorf method. *Solid State Ionics* **53**, 1087-1094 (1992).
24 Hafezi, H. and Newman, J. Verification and analysis of transference number measurements by the galvanostatic polarization method. *Journal of the Electrochemical Society* **147**, 3036-3042 (2000).
25 Ma, Y. P. *et al.* The measurement of a complete set of transport-properties for a concentrated solid polymer electrolytes solution. *Journal of the Electrochemical Society* **142**, 1859-1868 (1995).
26 Doyle, M., Fuller, T. F. and Newman, J. The importance of lithium ion transference number in lithium polymer cells. *Electrochimica Acta* **39**, 2073-2081 (1994).
27 Doyle, M., Fuller, T. F. and Newman, J. Modeling of galvvanostatic charge and discharge of the lithium polymer insertion cell. *Journal of the Electrochemical Society* **140**, 1526-1533 (1993).
28 Doeff, M. M., Edman, L., Sloop, S. E., Kerr, J. and De Jonghe, L. C. Transport properties of binary salt polymer electrolytes. *Journal of Power Sources* **89**, 227-231 (2000).
29 Edman, L., Doeff, M. M., Ferry, A., Kerr, J. and De Jonghe, L. C. Transport properties of the solid polymer electrolyte system P(EO)(n)LiTFSI. *Journal of Physical Chemistry B* **104**, 3476-3480 (2000).